Macromolecules

pubs.acs.org/Macromolecules

Article

Probing Three Distinct Crystal Polymorphs of Melt-Crystallized Polyamide 6 by an Integrated Fast Scanning Calorimetry Chip System

Xiaoshi Zhang, Anne Gohn, Gamini Mendis, John F. Buzinkai, Steven J. Weigand,
and Alicyn M. Rhoades*

Cite This: *Macromolecules* 2021, 54, 7512−7528

Read Online

ACCESS | Metrics & More | Article Recommendations | Supporting Information

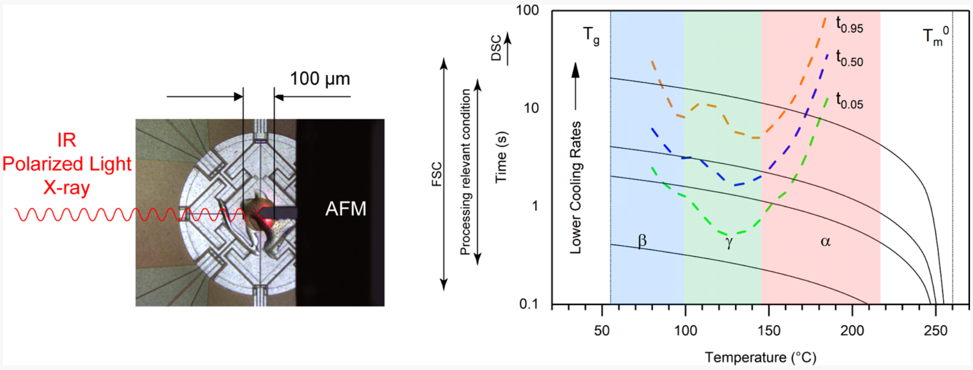

ABSTRACT: Isothermal crystallization of polyamide 6 (PA6) was studied using a state-of-the-art modified fast scanning calorimetry (FSC) chip over a wide temperature range. Microfocus FTIR spectroscopy was carried out to collect temperature-dependent spectra of PA6 directly on the FSC chip. The changes observed in amide- and methylene-related bands provide direct evidence of three crystalline modifications in PA6 from melt crystallization. The melt-crystallized PA6 was found to develop the mesomorphic β-phase below 105 °C and the α-phase above 150 °C. It has been confirmed that the γ-phase coexists with the β- or α-phase in the temperature region between 105 and 150 °C. Isothermal crystallization kinetics of PA6 in a wide temperature range were extracted directly from exothermic peaks and indirectly using the interruption method. A peculiar discontinuity in crystallization kinetics has been found in the transition region between the β- and γ-phases. In the same temperature region, a sudden transition from crystal aggregates to spherulitic morphology was captured by AFM. PA6 was cooled at rates from 10 to 2000 K/s before isothermal crystallization to mimic a full range of processing relevant conditions. A time−temperature−transformation diagram was built based on kinetic data to illustrate that the isothermal crystallization of PA6 is sensitive to the crystallization pathway. The novel platform built on a modified FSC chip is a powerful tool for the comprehensive study of polymer crystallization at processing-relevant conditions.

■ INTRODUCTION

Polyamide 6 (PA6) is one of the most successful commercial engineering plastics and is widely used in the automotive, aerospace, domestic appliance, and fiber industries. Like many other polymers, PA6 polymer chains, due to mobility restrictions in the melt, often do not organize into the thermodynamically most stable form during crystallization. As such, the formation of different crystal forms (polymorphs) is strongly dependent on crystallization kinetics or conditions.[1] In other words, the pathway that the polymer takes to crystallize may lead to the formation of entirely different crystalline forms with different thermal and dimensional stabilities, densities, and so forth.

To the best of the authors' knowledge, PA6 has been reported to have three polymorphs, α-, β-, and γ-phases. The α-polymorph, the thermodynamically most stable form of PA6, is easily accessible by either slowly cooling from the melt or through isothermal crystallization at low undercooling.[2,3] Another important polymorph of PA6, the γ-phase, can be prepared by KI/I_2 solution treatment of the α-phase[4] or can be grown from solutions.[5,6] The highly metastable β-phase can be prepared by fast melt-spinning at high speed[7] or quenching the

Received: April 13, 2021
Revised: July 1, 2021
Published: August 13, 2021

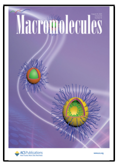

https://doi.org/10.1021/acs.macromol.1c00811

cast film on a chill roll, followed by annealing at a low temperature.[8,9]

Although PA6 is one of the most widely studied polyamides, it is also the subject of controversy and ambiguity with respect to structural configuration tendencies and thermodynamic properties in the literature, specifically with regard to the pseudo-hexagonal β- and γ-phases. As reviewed in a recent article by Seguela,[2] melt-spun fibers and blown and cast films of PA6 show characteristic wide-angle X-ray scattering (WAXS) patterns of the γ-phase.[10−13] The results of these studies are in good agreement with the structure of the γ-phase identified by Arimoto *et al.* from KI/I_2 solution-treated PA6.[4] A significantly more unstable form of PA6 with a similar WAXS pattern was also identified as the β-phase determined from a reorganization into the α-phase upon heating.[8,14,15] In contrast, Androsch and co-workers have only identified the α- and mesomorphic β-phases by either crystallizing from the melt[16] or cold crystallization from the glassy amorphous state.[17] It is possible that some of the identification of the γ-phase might be a misinterpretation of the β-phase because both phases have a characteristic WAXS pattern of the pseudo-hexagonal structure with a single strong reflection. Calorimetry studies have further supported this conclusion that the γ-phase in melt-spun fibers has multiple melting peaks as an indication of a continuous reorganization into a more thermally stable form,[13,18] while the solution-grown γ-phase does not undergo any crystalline transition on heating or cooling.[13,18,19] Hence, some authors also refer to the PA6 crystallized at low temperatures as the γ^*-phase to distinguish it from the most perfect γ-phase crystallized from solution.[10,20,21] The controversial assignment of the γ- and β-phase structure has led to a serious dispute about the Brill transition in PA6. The pseudo-hexagonal structure has been commonly observed in polyamides above the Brill transition. However, the existence and root causes of the Brill transition in PA6 are questioned due to the controversial experimental data.[18,22,23]

The contradictory observations regarding the two pseudo-hexagonal phases of PA6 are believed to be associated with the high sensitivity of polymorphic transitions to processing conditions. The formation of polymorphs in polyamides is always affected by the interplay between intermolecular hydrogen bonding from the amide groups and van der Waals interaction between the methylene segments. In PA-X-type aliphatic polyamides that have single numbers of $-CH_2-$ (*e.g.*, PA6, PA8, and PA12), the relative stability of the α-phase compared to the γ-phase depends strongly on the length of the methylene sequence. The γ-phase becomes more stable when the number of CH_2 units between amide groups is greater than or equal to seven, whereas the α-phase is more stable for PA6 or polyamides with shorter methylene segments.[24] It is noted that PA6 is a peculiar one in the series. Despite very different chain conformations and unit cells, α- and γ-crystals of PA6 were reported to have similar heat of fusion values for perfect crystals.[20,25] In addition, the *ab initio* calculation has also suggested that α- and γ-crystals are practically isoenergetic with an energy difference of only 0.045 kcal/mol per monomer unit.[24] The similar thermodynamic stability of α- and γ-crystals in PA6 results in the high sensitivity of polymorphic transitions to processing conditions.[23,26] The high sensitivity of PA6 to sample preparation makes the study of crystallization very challenging, especially for the low-temperature phase(s), because traditional methods cannot cool at controlled rates or avoid stretching and annealing during preparation. Although low-temperature isothermal crystallization can be achieved by quenching and subsequent cold crystallization from the glassy state, this may create different crystalline morphologies due to different nucleation mechanisms,[17,27] which does not reflect typical melt processing conditions.

Recently, with the advent of fast scanning calorimetry (FSC), owing to the extremely small sample size used on the sensor, heating and cooling can be achieved at rates up to 10000 K/s and 4000 K/s, respectively. The high scanning rate allows PA6 to be isothermally crystallized in a wide crystallization temperature range without "contamination" of other polymorphs during cooling.[16,17,28,29] The pioneering work by Androsch *et al.* using WAXS on FSC sensors successfully demonstrated that the mesomorphic β-phase and the thermodynamically stable α-phase can be prepared directly from the unoriented melt at high and low undercooling.[16,28] In one report, PA6 was also found to have a discontinuity, as indicated by an abrupt change in the curvature of the crystallization half-time versus temperature curve in its crystallization kinetics.[16] The kinetics discontinuity, as found in other polymers studied by FSC, including PA66,[30] PA11,[31] PBT,[32] iPP,[33] and PCL,[34] is often interpreted as either a change of the nucleation mechanism or a change of polymorphs.

Revealing the correlation between crystallization kinetics and different polymorphs of PA6 is of particular importance, especially in the low-temperature range where many ambiguous observations of β- and γ-phases are reported. The determination of a temperature region to demarcate different polymorphs has been demonstrated to be very challenging due to the intrinsic limitations of running WAXS on an FSC sensor. The sample mass used in FSC samples is usually in the submicrogram range, and the chip is sensitive to long-time beam damage.[16] Even with an intense microfocus synchrotron beam, the WAXS patterns collected directly on FSC chips always have a relatively low signal-to-noise ratio.[16] Perhaps more problematic, the mesomorphic and amorphous phases have a similar broad reflection with a d-spacing around 4 Å.[16,28,31] The shifting of the amorphous halo caused by thermal expansion proves especially challenging to separate from other crystalline peaks, especially near the pseudo-hexagonal phase/α-phase transition region, where two characteristic peaks of the α-phase merge into a single broad peak.[31,35] The characterization of polymorphism using WAXS requires sophisticated instrumentation and data processing. Alternatively, vibrational spectroscopy has been demonstrated to be highly efficient in following blue shifting caused by hydrogen bond changes between amide groups and conformation differences of methylene segments in different polymorphs of nylons.[12,15,23,24,36−38] Compared to WAXS that provides information regarding the crystallographic ordering, vibrational spectroscopy is more sensitive to the local conformation and interactions between polymer chains.

Herein, the work aims to establish a thorough understanding of the formation of different polymorphs crystallized from the melt and their associated crystallization kinetics, spectroscopic, and morphologic characteristics. This goal is achieved by using a novel integrated FSC chip that also allows vibrational spectroscopy characterization. The modified FSC chip also enables the authors for the first time to cool and heat PA6 samples at an ultrahigh rate to the desired temperature to perform nondamaging repeatable morphology characterizations on UFS1-type chips. Ultimately, a time−temperature-

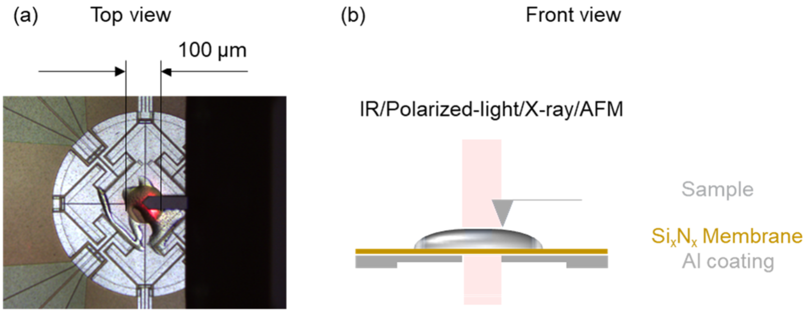

Figure 1. (a) Top view of a modified UFS1 sensor during AFM imaging. The center aluminum coating on the SiN_x membrane was removed to provide a 100 μm diameter opening (b) schematic front view of the modified UFS1 sensor (not to scale). The modified sensor supports nondamaging IR, polarized light, X-ray, and AFM experiments.

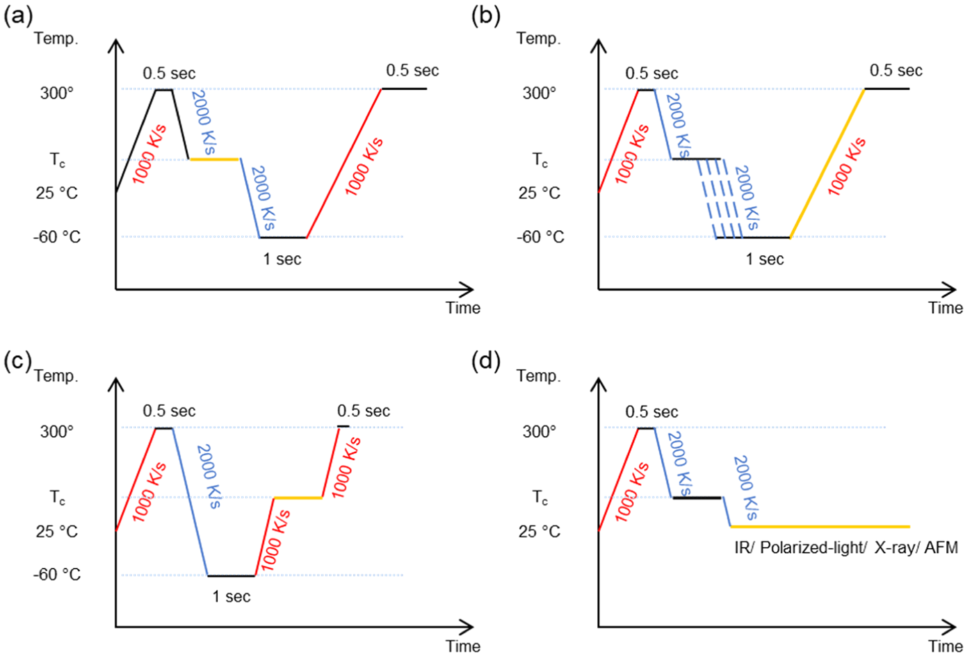

Figure 2. Temperature−time protocol used in the FSC for (a, b, c) isothermal crystallization analysis or (d) preparation. (a) Isothermal crystallization peak time directly measured from exothermic heat flow. (b) Half-transformation time extracted from the heat of fusion after interruption of the isothermal crystallization at predefined times. (c) Isothermal crystallization from the glassy state. (d) Modified UFS1 chip used as a micro hot stage for subsequent characterizations using other instruments. The measurements were carried out in the portion of each method highlighted yellow.

transformation (TTT) diagram was built based on the results collected on the FSC chip.

■ EXPERIMENTAL SECTION

Materials and Preparation. Commercial resin grade Ultramid B27E 01 from BASF was used for the study of PA6 crystallization. Ultramid B27E 01 is additive-free PA6 with a solution viscosity of about 2.7 RV for 1.0 w/v % solution in 96% sulfuric acid or VN of about 150 mL/g as determined by ISO 307 with 96% sulfuric acid. The estimated number-average molar mass is about 16 kg/mol. The as-received pellets were dried to 0.07% moisture prior to experiments. The PA6 pellets were then microtomed to obtain sections with a thickness of 20 μm. These thin sections were cut to obtain a lateral dimension of around 50−100 μm using a scalpel under a stereomicroscope.

Measurements. *Fast Scanning Calorimetry.* A modified UFS1 chip was used for calorimetry and subsequent spectroscopy, scattering, and morphology analyses. The chip has an active heating and cooling zone of 0.5 mm diameter at a membrane thickness of about 2 μm. As illustrated in Figure 1, the center aluminum coating was removed to provide a 100 μm diameter opening. The amorphous SiN_x membrane used on the UFS1 chip is functionally transparent to IR, except for the absorption bands at 1081 and 821 cm^{-1}, as shown in Figure S1. The aluminum coating was used to attain a uniform sample-area temperature,[39] so the removal of the aluminum coating may introduce a greater thermal lag during scanning than in the regular FSC chip. In order to assess the thermal lag in the modified chip, a standard chip was also used for comparison.

Sample preparation and calorimetric analyses were carried out using a Mettler Toledo Flash DSC 1 connected to a Huber TC100 two-step cooling intracooler. The FSC sensors were conditioned and temperature-corrected prior to loading the specimen. In all instances, the calorimeter was purged with dry nitrogen gas. Thin specimens were directly loaded on the center of the chip and then prepared in their molten state inside the FSC. In order to obtain the optimal IR spectra, the thickness of the sample is further reduced by using a thin wire to spread molten PA6 over the heating zone. The entire operation is conducted under nitrogen flow to minimize the possibility of degradation. No bands associated with degradation[40] were found in the spectra collected after sample preparation. Similar sample preparation has been reported by Anton *et al.* in their work on PA66.[41]

For obtaining kinetics information, the PA6 sample was initially heated to 300 °C (higher than reported $T_{m,0}$ of PA6, 260 °C[10]) for 0.5 s to erase thermal history. Then, the melt was cooled to the crystallization temperature (T_c) at a rate of 2000 K/s. Depending on the signal-to-noise ratio of the exothermic heat flow, two different types of temperature−time protocols were adapted to analyze the isothermal kinetics for melt crystallization as illustrated in the (a) and (b) panels of Figure 2. When the exothermic heat flow was distinguishable from noise, the sample was maintained at the selected isothermal crystallization temperature for 30 s to ensure complete crystallization. The high signal-to-noise ratio allows us to measure the exothermic peak time directly. When the crystallization process is slow, the kinetics can be determined by interruption of the isothermal crystallization process at predefined crystallization times, followed by rapid cooling to below the glass transition temperature (T_g) at a rate of 2000 K/s. The rapidly cooled samples were then melted at a rate of 1000 K/s to measure the heat of fusion. The half-transformation time, $t_{0.5}$, can then be extracted from a conversion-time $y-t$ plot using a four-parameter logistic equation given below,[42] where $a_{\min}$ and $a_{\max}$ are conversions at time 0 and infinity, respectively, and p is the fitting power.

$$y = a_{\min} + \frac{a_{\max} - a_{\min}}{1 + (t_{0.5}/t)^p}$$

The scanning rates used in the interrupted methods were fast enough to bypass melt crystallization and cold crystallization of PA6, as displayed in Figure S2. The protocol shown in Figure 2c was used to extract crystallization kinetics from cold crystallization.

The FSC chip was also used as a micro hot stage for subsequent WAXS/FTIR spectroscopy/polarized optical microscopy (POM)/AFM experiments, as illustrated in panel (d) of Figure 2. The samples were melted at 300 °C for 0.5 s to eliminate thermal history and then cooled to the isothermal crystallization temperature at 2000 K/s and maintained for 2 min to ensure full transformation. The samples were then quickly quenched to 25 °C, which is below the glass transition temperature of PA6, at a cooling rate of 2000 K/s. The fast cooling process freezes the material structure developed at a given crystallization temperature. Then, the sample on the sensor was transferred into a different instrument for measurements. After measurements, the sensor and sample were reinserted into the FSC for subsequent thermal treatment.

Wide-angle X-Ray Scattering. The WAXS measurements of the preconditioned FSC samples were carried out on an in-house Xenocs Xeuss 2.0 small-angle X-ray scattering (SAXS)/WAXS instrument equipped with a Pilatus 200K detector and collimation optics. A Cu Kα source (λ = 1.54 Å) was used for the experiments. A standard sample of silver behenate was used for the calibration. All diffractograms of the samples and FSC reference chips were collected with an accumulated exposure time of 1800 s.

Simultaneous Synchrotron X-ray. SAXS, middle-angle X-ray scattering, and WAXS experiments were carried out using beamline 5ID-D of the Dupont-Northwestern-Dow Collaborative Access Team Synchrotron Research Center at the Advanced Photon Source, Argonne National Laboratory. Simultaneous 2D patterns were collected using an exposure time of 1 s at room temperature. The 2D patterns were azimuthally averaged to 1D patterns. The patterns are shown as a function of the scattering vector, q ($q = 4\pi \sin \theta/\lambda$, where 2θ is the scattering angle and λ = 0.7293 Å), measured in the range of 0.0025−4.46 Å^{-1}.

FTIR Spectroscopy. FTIR spectra were collected using Bruker Hyperion 3000 micro-IR equipped with a liquid nitrogen-cooled mercury−cadmium−telluride detector and a Bruker Vertex 70 FTIR spectrometer. The data acquisition and analyses were carried out using OPUS 7.0 provided with the instrument. The spectra were collected in absorption mode in the wavenumber range between 7500 and 400 cm^{-1}. Per spectrum, 64 scans were run at a resolution of 2 cm^{-1}. As displayed in Figure S1, a spectrum of the amorphous SiN$_x$ membrane contains two bands at 1081 and 821 cm^{-1}. In addition to these two bands, multiple broad sinusoidal bands (fringes) in the range of 7500−2000 cm^{-1} were also observed. The fringes, also called Fabry−Perot fringes, are caused by the multiple interferences between beams transmitted and partially reflected at the film−substrate interfaces.[43] In this study, the extended multiplicative signal correction approach was followed to correct the fringes in the mid-IR range.[44,45] An example of the removal of fringes is illustrated in Figure S1.

Polarized Optical Microscopy. The polarized micrographs of PA6 were collected directly on the chip using a Leica DM2700P microscope and a Leica DFC7000T camera in transmission mode. A retardation plate was also used to enhance the contrast in weakly birefringent spherulites. The POM images were processed and analyzed using ImageJ from the National Institutes of Health.

Atomic Force Microscopy. A Bruker Dimension ICON atomic force microscope with a NanoScope V controller was employed to perform imaging directly on the chip with PeakForce QNM mode at ambient temperature. The samples were scanned using a ScanAsyst-Air probe with a tip radius of 2 nm, a nominal resonant frequency of 70 kHz, and a nominal spring constant of 0.4 N/m. Height, height error, and peak force error channels were collected. The AFM images were processed and analyzed using NanoScope Analysis Software provided by Bruker.

RESULTS AND DISCUSSION

Polymorphism in PA6. The WAXS diffractograms were recorded on the chip after isothermal crystallization at 100 and 180 °C, as displayed in Figure 3. The peak at 28.5° results from the FSC chip membrane and is not important for analysis. With regard to the PA6 samples, major differences are apparent between crystalline phases formed at high and low temperatures. The WAXS pattern of PA6 crystallized at 180 °C contains two major peaks at 20.3 and 23.9°, associated with the diffraction of (200) and (002)/(202) planes of the α-phase,[46] respectively, whereas the diffractogram collected after crystallization at 100 °C has a broad diffraction peak located at 21.6°, characteristic of PA6 mesophase (β-phase).[7,8] It is noted that a single diffraction peak also characterizes the major reflection (200)/(001) of the PA6 γ-phase.[4] Unlike the peak of the γ-phase that is sharp and intense, this study's broad diffraction is closer to the previously studied β-phase.[8] Besides, the low-temperature diffractogram of PA6 does not have the (020) diffraction peak of the γ-phase[4] in the low 2θ region. Our observation is consistent with previous work on melt-crystallized PA6 using microfocus synchrotron WAXS[16] that β- and α-phases form at 95 and 180 °C, respectively.

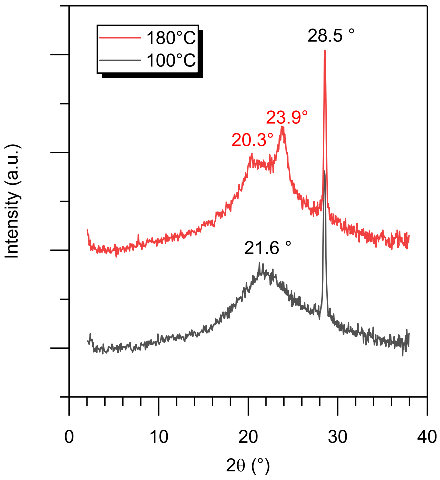

Figure 3. WAXS patterns of the PA6 α-phase and β-phase isothermally crystallized at 180 and 100 °C, respectively.

The WAXS patterns collected directly on FSC chips using either in-house or synchrotron X-ray have a relatively low signal-to-noise ratio. In addition to this problem, the mesophase and amorphous phase have a similar broad reflection with a d-spacing around 4 Å as previously reported in PA6,[28] PA11,[31] and polyacetals.[47,48] The shifting of the amorphous halo caused by thermal expansion/shrinkage makes it more challenging to separate from other reflections, especially near the pseudo-hexagonal phase/α-phase transition region, where two characteristic peaks of the α-phase merge into a single broad peak. Thus, the determination of the transition region in PA6 requires high-quality WAXS patterns, a reasonable estimation of halo shifting, and precise deconvolution of different polymorphs. Many authors have already discussed the difficulty of separating polymorphs in nylons using X-ray diffraction data.[15,16,49] Although the limitation of signal-to-noise issues may be overcome by the synchrotron photon source, repeated exposure of the FSC sensor to intense X-ray radiation could lead to beam damage.[16]

Microfocus FTIR offers an alternative route to differentiate between polyamide polymorphs. Vibration spectroscopy has been highly instrumental in following frequency shifting caused by hydrogen bond changes between amide groups and conformation differences of methylene segments in different polymorphs of PA6.[12,15,23,24,36−38] Previously, many researchers struggled to obtain the spectra of pure crystalline modifications of PA6.[15,23,37] In this study, owing to the fast cooling rate of the FSC and the novel modified FSC chip, the spectra of pure melt-crystallized α-, γ-, and β-phases of PA6 were identified for the first time. The spectra were normalized by the intensity of the amide I band at 1641 cm^{-1}. The changes in the frequency and normalized absorbance values occur at almost the same temperature for bands discussed below. Hence, the changes are divided into three temperature regions: below 105, 105−150 °C, and above 150 °C. The representative spectra for the three temperature regions at 80, 130, and 180 °C are shown in Figure 6 for illustration. For comparison purposes, a spectrum of the amorphous phase was prepared by quenching PA6 from 300 to 25 °C at the same cooling rate of 2000 K/s and is also included in the same figure. An example of absorbance deconvolution is displayed in the left panel of Figure 6. The frequencies and assignments of major bands of PA6 α-, γ-, and β-phases are summarized in Table S1.

Four major amide-associated bands at around 3300 cm^{-1} (hydrogen-bonded N−H stretching), 3085 cm^{-1} (N−H Fermi resonance of N−H stretching with the overtone of amide II), 1641 cm^{-1} (amide I, C═O stretching), and 1550 cm^{-1} (amide II, coupling of C−N stretching with N−H in-plane bending mode) are identified for all spectra displayed in Figure 4. The hydrogen-bonded N−H stretching band at 3300 cm^{-1} has similar frequency values in the temperature range between 80 and 105 °C. This band quickly shifts to a lower frequency with increasing T_c, reaching its minimum at 3295 cm^{-1} at a temperature of 130 °C. Then, this band shifts back to around 3302 cm^{-1} at 150 °C and remains unchanged for the remaining values of T_c. The lower frequency observed in the spectrum of 130 °C than in the spectrum of 180 °C indicates stronger hydrogen bonding between adjacent amide groups. A similar variation of the H-bond-related band has been predicted by DFT calculation, showing that the γ-phase has a slightly lower frequency than the α-phase.[24] Although several authors conclude that the H bonding in the α-phase is stronger than in the γ-phase based on better thermal stability, the *ab initio* calculation and previous IR measurements have concluded that H bonding is stronger in the γ-phase than in the α-phase.[50−52] Shifting of the other N−H stretching bands also occurs with varying T_c. Blue shifting was previously found to occur for the amide II-associated bands during α- to γ-phase transition in nylons.[37,53] A similar shifting from 1545 to 1552 cm^{-1} is found in the spectra after changing T_c from 180 to 130 °C, and then, the peak shifts slightly back to 1550 cm^{-1} with further decreasing T_c to 80 °C. The shifting is also reflected in the amide II band's overtone by changes in frequency from 3075 to 3089 cm^{-1} and then back to 3085 cm^{-1}.

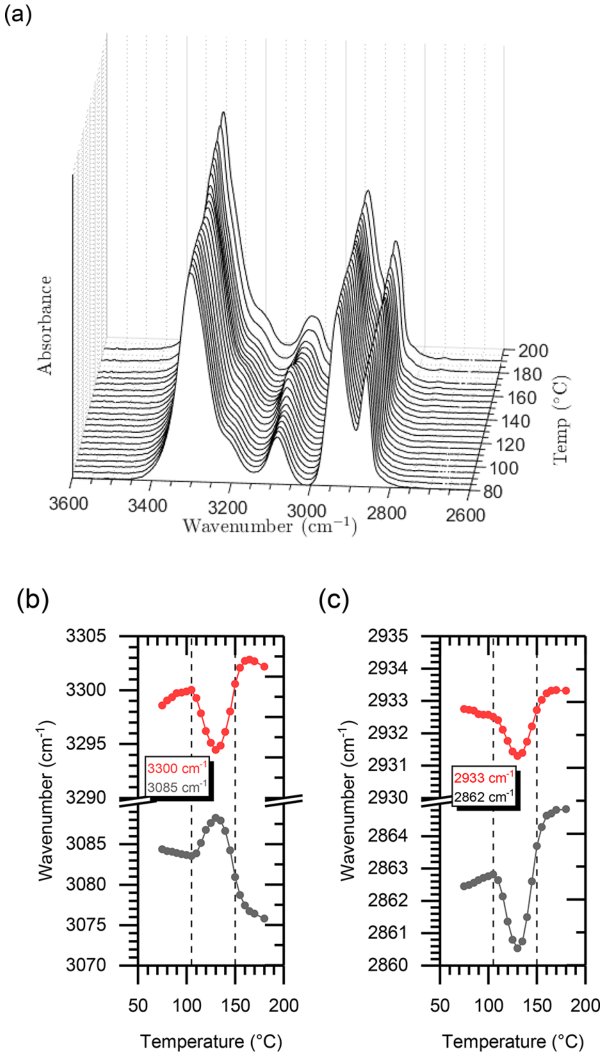

Figure 4. (a) FTIR spectra in the region 3600−2600 cm^{-1} of PA6 after isothermal crystallization at the indicated temperature. Variation in the wavenumber of (b) amide-related bands and (c) CH$_2$ stretching bands.

The methylene-related bands also reflect the formation of different polymorphs in three different temperature regions. As shown in Figure 4, the observation of low frequencies of CH stretching bands in the spectra collected near 130 °C is again characteristic of the spectrum of iodine solution-prepared γ-phase.[24] In both cases, it was found that the two broad bands of the γ-phase have lower frequencies than the two bands of the α-phase. In the CH$_2$ scissoring region between 1500 and 1400 cm^{-1}, the bands at 1474 and 1417 cm^{-1} are correlated with methylene scissoring mode from methylene groups adjacent to the amide group in *trans* conformation as summarized for PA6[37,54] and PA66,[55,56] while the band at 1440 cm^{-1} is interpreted as the rotation of the $-CH_2-CONH-CH_2$ group out of the ideal *trans* conformation,[56] which has been seen in the quenched PA6 film[57] or iodine solution-treated PA6[37] associated with the β- and γ-phase, respectively. Additionally, the band at 1463 cm^{-1} is attributed to the nonamide vicinal methylene.[56,58] As shown in Figure 5, four peaks at about 1476, 1462, 1437, and 1418 cm^{-1} appear when T_c is above 140 °C. Among the four bands, the band at 1438 cm^{-1} has the lowest intensity and remains basically unchanged in the high-temperature region. Below 140 °C, the spectra show only two major absorption bands at 1440 and 1463 cm^{-1}, suggesting they no longer have *all-trans* chains. The band at 1440 cm^{-1} associated with the nonplanar structure reaches its maximum at 130 °C. Its intensity then decreases with increased undercooling. When the temperature is below 105 °C, this band remains unchanged but still has a higher intensity than observed above 130 °C. The results show good agreement with the chain models proposed for the three crystalline modifications of PA6 that the dihedral angles adjacent to the amide groups (θ) are 180 and 120° for the α-[46,59] and γ-phase,[4] respectively, while the θ values for the β-phase vary in the range of 120−180°.[7] The vibration band at 1463 cm^{-1}, assigned as nonamide vicinal methylene scissoring mode, also varies for different crystalline modifications, as shown in Figure 5. In the model of the α- and γ-phase,[4,46,59] the nonamide vicinal methylene has *all-trans* conformation. The similar absorbance of this band at 130 and 180 °C indicates that they both have high regularity. The continuous decrease of the 1463 cm^{-1} band with lower T_c in the mesomorphic β-phase region suggests a more disordered conformation than the other two phases. In the β-phase model proposed by Auriemma *et al.*,[7] conformations of the chain are adjusted with some degrees of conformation disorders to have amide groups nearly at the same height along the chain direction to form H-bond layers. Using the reported crystalline structure of the three phases,[7,37,46,59] the conformation information regarding the methylene sequence for α-, γ-, and β-phases is shown in Figure 7.

In the spectral region between 1350 and 1150 cm^{-1}, the bands at 1260 cm^{-1} (CH_2 wagging) and 1206 cm^{-1} (CH_2 wagging) characterize the formation of the α-phase.[23,37] On the other hand, the band at 1235 cm^{-1} (CH_2 twisting) was found to be predominant in the γ-phase.[37,60,61] The spectrum of 180 °C again has all the α-phase features, while the low-temperature spectrum of 130 °C shows a relatively strong 1235 cm^{-1} band. Besides, the band at 1170 cm^{-1} (CH_2 twisting), usually assigned as a reference band in former studies,[12,36] shows a much higher intensity in the spectra of 130 °C than the one observed in 80 and 180°C spectra. Both ratios of bands at 1237/1256 and 1170/1206 cm^{-1} reach their maximum at around 130 °C.

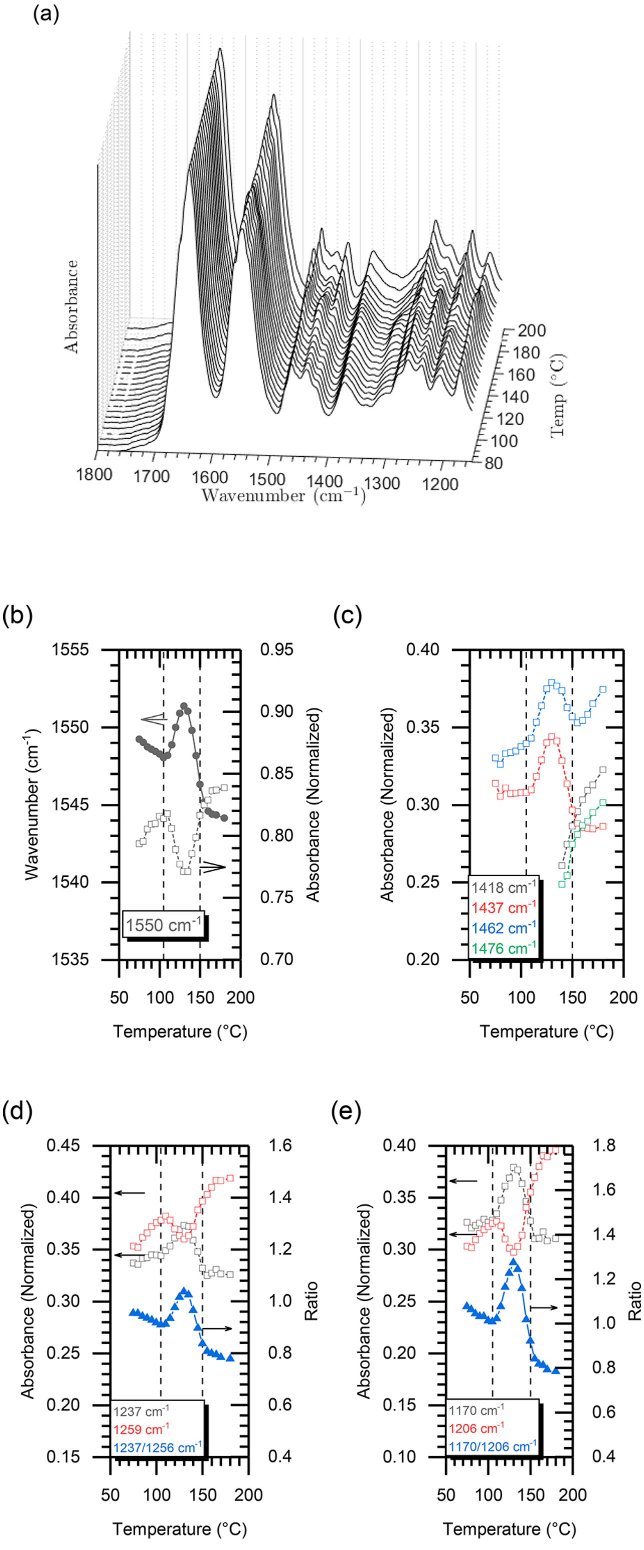

Figure 5. (a) FTIR spectra in the region 1800−1150 cm^{-1} of PA6 after isothermal crystallization at the indicated temperature. Variation of the wavenumber and normalized absorbance of the (b) amide II band. Variation of normalized absorbance of (c) CH_2 scissoring bands, (d) bands at 1237 and 1259 cm^{-1}, and (e) bands at 1170 and 1206 cm^{-1}. The absorbance ratios of 1237/1256 and 1170/1206 cm^{-1} are plotted in (d,e).

Following the discussion above, the PA6 crystallized above 150 °C clearly forms an α-phase. Although the spectra of low-temperature PA6 crystals show many similarities, after careful evaluation, it is clear that they exhibit slight differences for many amide-related and methylene-related bands. The spectrum of the sample crystallized at 130 °C has sharper bands at 3085, 2862, 1462, 1437, 1237, and 1170 cm^{-1} compared to the spectrum of 80 °C. Besides, the single band at 1204 cm^{-1} in PA6 that crystallized below 105 °C splits into a major band at 1204 cm^{-1} and a shoulder at 1211 cm^{-1} in the temperature region between 105 and 150 °C, which is similar to the observation from the KI/I_2 solution-treated PA6 γ-

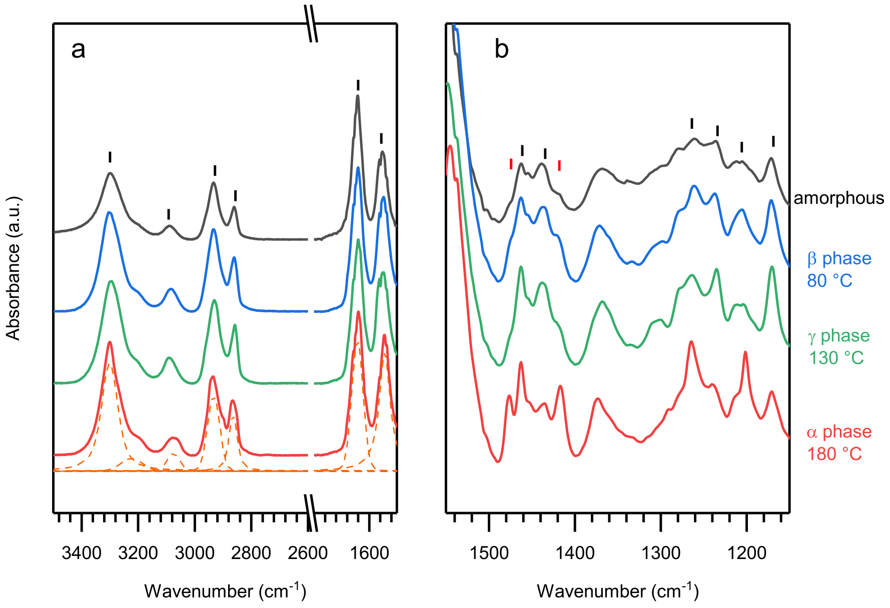

Figure 6. Representative FTIR spectra in the regions (a) 3500−1500 and (b) 1600−1100 cm^{-1} of PA6 taken at indicated temperatures for the amorphous phase, β-, γ-, and α-phases. All the discussed bands are marked with bars.

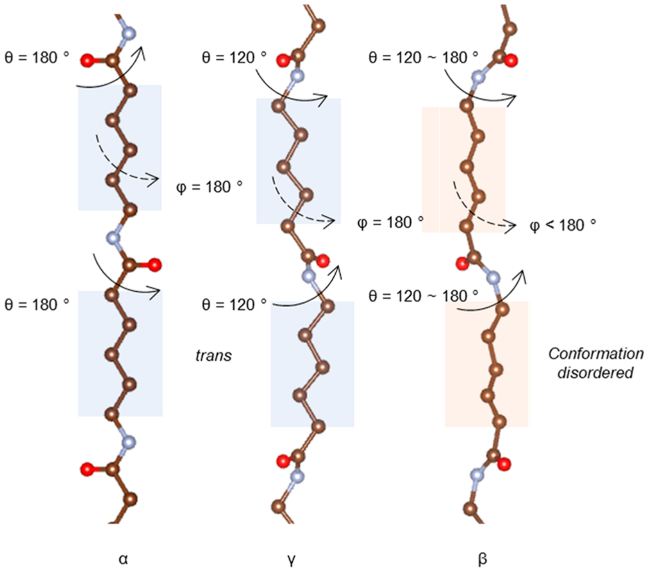

Figure 7. Chain models proposed for PA6 α-, γ-, and β-form. The values for the dihedral angles adjacent to the amide groups (θ) are 180 and 120° for the α- and γ-phase, respectively, while the θ values for the β-phase vary in the range of 120−180°. The dihedral angle for nonamide vicinal methylene sequences (φ) is 180° for α- and γ-phases. The β-phase exhibits disordered conformation with nearly *all-trans* for the methylene chains.

phase.[24,38] The merging of the two peaks at lower T_c is caused by the low symmetry of the crystal structure as predicated in the β-phase structure. In a structure containing low symmetry, such as the rotator phase, the molecule rotates around the chain axis, and the motion will average to a broader band as seen in the spectra. The splitting of vibration bands has been observed in a large number of polymorphs in polymers and oligomers, for example, from the triclinic phase to the orthorhombic phase in polyethylene (PE),[62] PE-like polymers,[63] and *n*-paraffins.[64] Furthermore, compared to the spectrum at 80 °C, the bands at 1552, 3089, and 2862 cm^{-1} in the spectrum of 130 °C deviate even more from the spectrum of the α-phase instead of having frequency values in between, indicating more conformation differences. This is consistent with the previous discussion by Penel-Pierron *et al.*, who pointed out that the β-form is the intermediate structure between the α-phase and γ-phase from the standpoint of hydrogen bonds and conformation.[15] The observation of sharpening, splitting, and shifting of bands in the spectra obtained in the 105−150 °C region suggests that a more γ-like structure is formed in this temperature range. More importantly, the abrupt changes in frequency and absorbance that occur near 105 °C provide direct evidence that the γ-like structure is not a β-form with gradually increasing symmetry of the chain conformation. Instead, the formation of the γ-like structure is triggered by a sudden change in chain packing. The spectrum collected at 130 °C exhibits all the features seen in the γ-phase prepared by KI/I_2 solution.[24,38]

The formation of the γ-phase at 130 °C has also been confirmed by using synchrotron X-ray scattering. As displayed in Figure 8, the diffractogram shows a sharper reflection at q of 1.51 Å^{-1} that corresponds to the (200)/(001) plane of the γ-phase. Besides, the (020) plane of the γ-phase can be seen at around 0.78 Å^{-1}. Previous work by Xu *et al.* has demonstrated that the lamellar peak can only be seen in the α- and γ-phase of PA6.[65] The weak lamellar peak observed at q of 0.08 Å^{-1} confirms the formation of the γ-phase. In this study, the crystals formed at 130 °C will be designated as the γ-phase to distinguish them from the β-phase that is formed below 105 °C. Temperature-dependent FTIR spectra provide direct evidence of the existence of three crystalline phases by melt crystallization. The β-phase crystallizes below 105 °C and the α-phase crystallizes above 150 °C. In the intermediate temperature region, the γ-phase coexists with the β- or α-phase.

Overall Isothermal Crystallization Rates. The evolution of the isothermal heat flows with increasing crystallization temperature obtained from PA6 is displayed in Figure 9. The peak of each thermogram indicates the highest exothermic heat flow during crystallization. The time to reach the exothermic

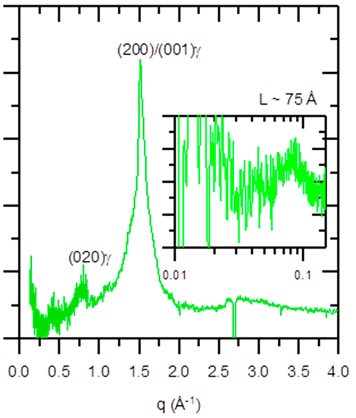

Figure 8. Synchrotron WAXS pattern of the PA6 γ-phase isothermally crystallized at 130 °C. The diffraction peaks at 0.78 and 1.51 Å^{-1} are the (020) and (200)/(001) planes of the γ-phase. The SAXS pattern is displayed as an inset to show a weak lamellar peak at q of 0.08 Å^{-1}.

peak, named crystallization peak time (t_{peak}), can be regarded as half-transformation time ($t_{0.5}$) if the exothermic crystallization peak is relatively symmetric. According to the Turnbull–Fisher equation,[66] crystallization time usually decreases with increasing thermodynamic drive at higher undercooling. Then, the decreasing mobility of chain segments at low temperatures becomes the dominant factor, causing t_{peak} to pass a minimum and then increase on the approach of glass transition temperature T_g. A single t_{peak} minimum can be obtained in polymers that only exhibit a single polymorph, such as PEEK.[67] However, the melt-crystallized PA6, as shown in Figure 9, has very unusual crystallization kinetics behavior, especially in the low-temperature region where the β- and γ-phases develop. In the region from 180 to 160 °C, where only the α-phase crystallizes, all the exothermic peaks have a relatively symmetric shape. As expected, t_{peak} gets shorter at lower crystallization temperatures. When the temperature decreases to 160 °C, the long tail of the exothermic peak becomes more apparent, causing the peak to become more asymmetric. The change of t_{peak} and the peak shape continues until reaching a minimum at around 130 °C. It is noted that this is also the temperature that has the highest content of the γ-phase. Then, a discontinuity region is identified in the temperature region between 100 and 130 °C. In this temperature region, the crystallization curve no longer has a well-defined single exothermic peak. Instead, an overlap of two peaks associated with the coexistence of two polymorphs can be identified. On the lower temperature side of the discontinuity region, a symmetric exothermic peak appears again, denoting the formation of only the β-phase. Upon further increasing undercooling in the low-temperature region, the time for crystallization progressively increases and follows classical nucleation theory. The abovementioned observations are reproducible on a regular chip, as displayed in Figure S3.

The crystallization kinetics data were extended to a broader temperature range by interrupting the isothermal crystallization process at predefined crystallization times. An example of six sets of FSC melting curves is shown in Figure 10 for crystallization between 80 and 180 °C with different hold times. Their corresponding variations in enthalpy of fusion as a function of hold time are also displayed in the same figure. In all the temperatures studied, the flat black line corresponding to 0.1 s of crystallization confirms that the cooling rate and heating rate are fast enough to bypass any crystallization during thermal scanning, while the orange and red curves indicate that the transformation is basically completed after 60 s, except for some crystal/lamellar-thickening-related shifting of the melting peaks. The melting curves can be divided into the same temperature regions for β-, γ-, and α-phases, as discussed previously.

The crystallization time in a broad temperature range between 80 and 190 °C is displayed in Figure 11. Because the measurement of t_{peak} has a high degree of uncertainty, the

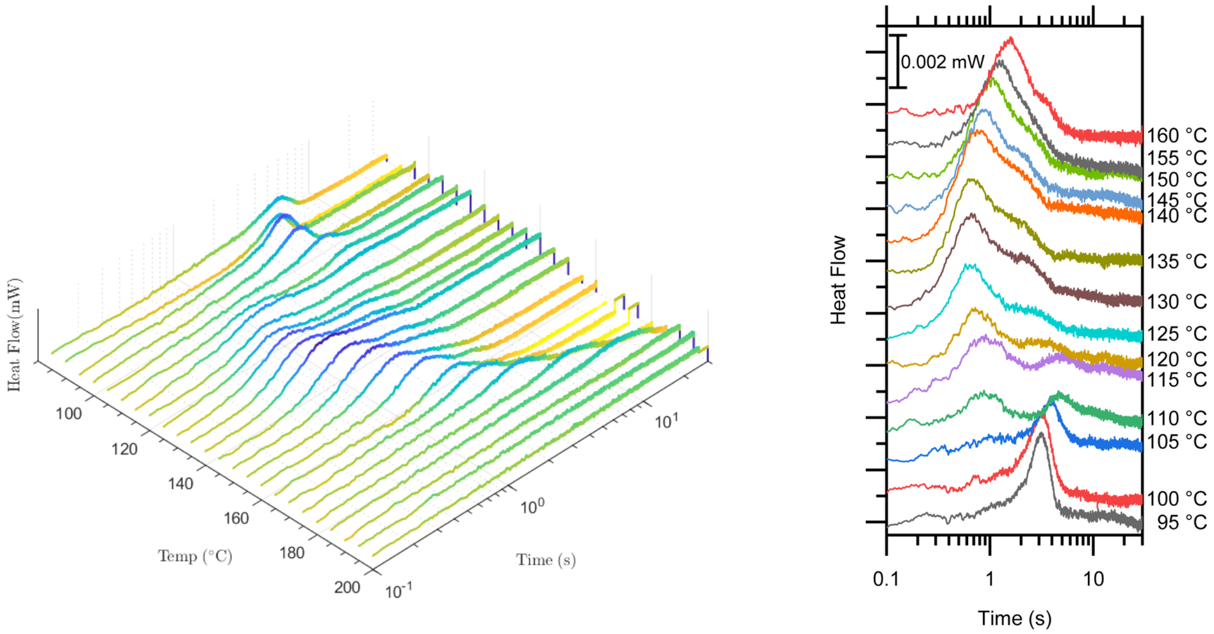

Figure 9. (Left) Waterfall plot of the heat flow rate as a function of time, obtained during isothermal crystallization of PA6 at temperatures between 80 and 200 °C. The exothermic heat flow is positive (directed upward). (Right) Heat flow during isothermal crystallization at temperatures between 95 and 160 °C.

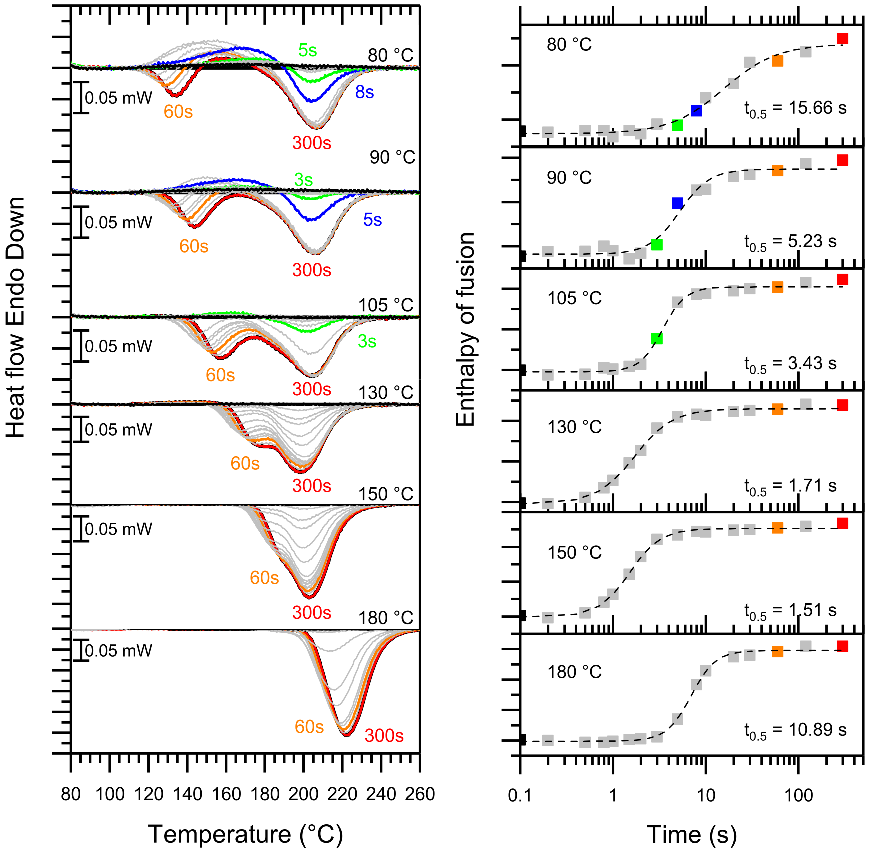

Figure 10. (Left) Melting curves after crystallization at indicated temperatures with predefined crystallization times from 0.1 to 300 s. (Right) Variation of the heat of fusion with time. The $t_{0.5}$ value was extracted with the logistic equation. The same colors are used in melting curves and their corresponding enthalpy of fusion values.

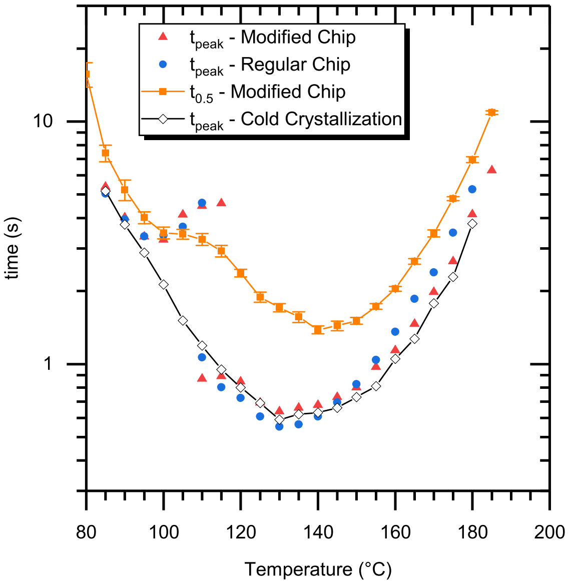

Figure 11. Crystallization time of PA6 as a function of the crystallization temperature. The plot includes data collected using three different protocols as described in the text.

average values were calculated from five regular chips and three modified chips. The two sets of the t_{peak} average data show relatively good agreement; therefore, the thermal lag in the modified chip is negligible compared to the regular chip. The t_{peak} and $t_{0.5}$ values extracted from different methods are also compared. It is noted that t_{peak} only depends on the crystallization rate of one polymorph, while the $t_{0.5}$ value is extracted from overall crystallization regardless of the number of phases. The t_{peak} and $t_{0.5}$ values overlap when the temperature is below 105 °C because only the β-phase crystallizes in this region. At 105 °C, the two values start to deviate. Surprisingly, the β-phase formation starts to slow down even though the crystallization temperature is only 40 °C above T_g. Meanwhile, $t_{0.5}$ remains unchanged at 105 °C, which can only be explained by the formation of another phase with faster kinetics. The gap between the two sets of values enlarges drastically when the temperature is above 110 °C. In the t_{peak} data, the crystallization time undergoes a step decrease from about 4 s at 105 °C to 1 s at 110 °C, while $t_{0.5}$ only shows a continuous bimodal dependence of crystallization against temperature. These t_{peak} data suggest that the newly formed γ-phase exhibits a much faster crystallization rate. To our knowledge, such a step change of the crystallization time has only been previously found in carbon nanotube-filled iPP at mesophase/α-phase polymorphism transition temperatures.[68] With increasing temperature, t_{peak} and $t_{0.5}$ reach their minima at 130 °C and 140 °C, respectively. The gap between t_{peak} and $t_{0.5}$ gradually narrows after entering the α-phase region. Our observation of crystallization time $t_{0.5}$ is in good agreement with previous data reported by van Drongelen *et al.*[16] that melt-crystallized PA6 shows a bimodal time−temperature dependence. In contrast, the t_{peak} data of PA6 extracted from cold crystallization only show a monomodal distribution of the overall rate. No t_{peak} step change is observed at the β-/γ-phase

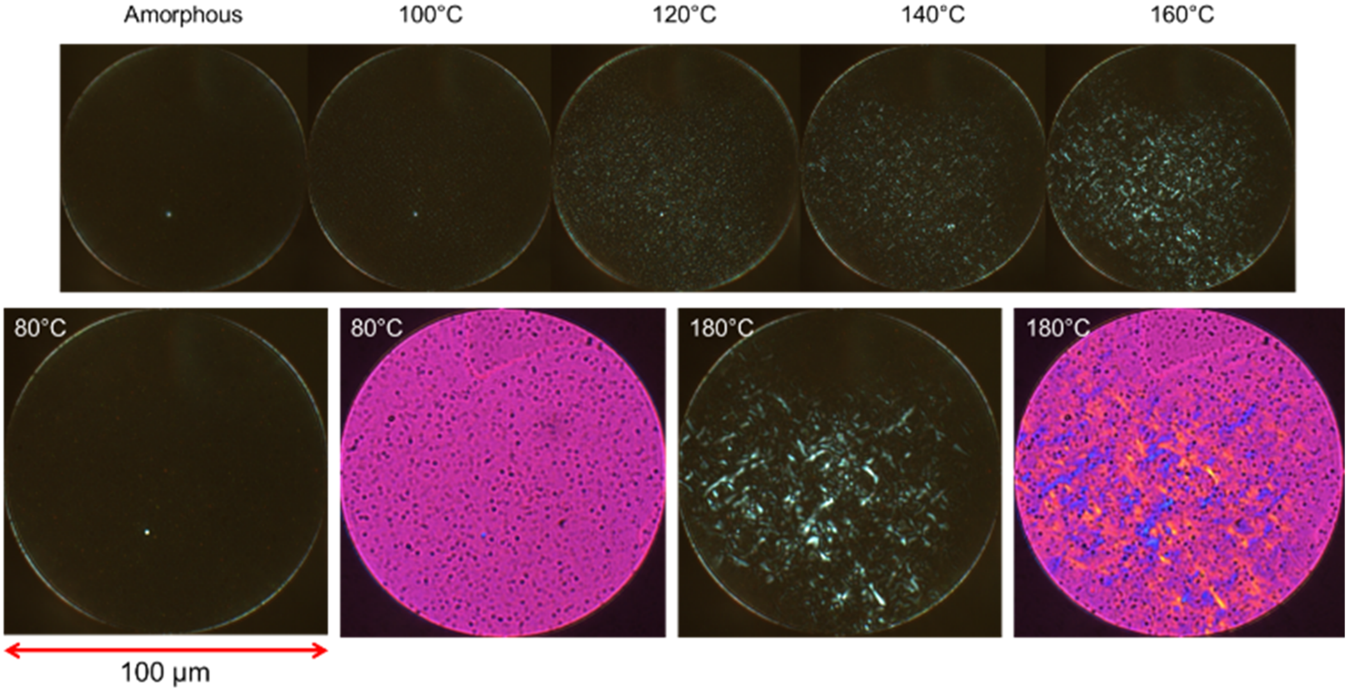

Figure 12. Representative polarized optical micrographs of PA6 isothermally crystallized at indicated temperatures. The opening on the modified chip for imaging is 100 μm. The large images were obtained on samples crystallized at 80 and 180 °C. A retardation plate is used to enhance the contrast.

transition region, as shown in Figures 11 and S3. Except for the transition region, the t_{peak} values measured by melt and cold crystallization are in good agreement. Our observation is consistent with previous data by Kolesov *et al.*[49] The difference in kinetic data generated by two approaches using melt or cold crystallization clearly indicates the importance of the crystallization pathway. Hence, it is essential to follow the same path to crystallize or prepare the samples in order to mimic real melt processing.

The occurrence of peculiar crystallization kinetics with discontinuities has been widely found in many polymers that develop the mesophase, including PA66,[30] PA11,[31] PBT,[32] iPP,[33,68] PCL,[34] and so forth, owing to the fast temperature control and data acquisition of the FSC. Not only in those samples studied by the FSC but crystallization rate discontinuity has also been reported in polymers that exhibit slow crystallization kinetics, such as sPS,[69] PLA,[70] PE-like oligomers, and polymers.[48,71−73] The mechanism that leads to discontinuity is still under debate.

The reason for the crystallization discontinuity may be related to polymorphs or conformational changes. This idea has been widely investigated by the crystallization study of PE-like polymers and oligomers.[48,71−76] The crystallization rate minimum was first obtained by Ungar *et al.* in their study of long-chain *n*-alkanes crystallized from the melt and solution.[71,74−76] Long-chain *n*-alkanes can develop in extended forms or integer folded forms with increasing undercooling. The relative stability of the different forms also follows the Gibbs−Thompson equation that the extended form has a higher melting temperature than the folded form. In the temperature region where the folded form transfers to the extended form, a deep minimum was obtained. The peculiar crystallization kinetics behavior was explained by the manifestation of self-poisoning. In the narrow transition region, the lamellar growth of the extended form is temporarily blocked by the less stable folded form. Because the stable form has a longer lamellar thickness, it cannot grow on the folded chain substrate. The less stable form must be detached in order to continue the growth of the extended form. Recently, Alamo and co-workers have observed a similar crystallization minimum in precision PEs that have equidistant placement of a counit along the backbone.[48,73] In the precision PEs, the stability of the polymorphs is directly associated with chain conformation rather than different lamellar thicknesses. It was also confirmed that the less stable form has a much higher nucleation rate than the more stable form.[48,73] In the proposed mechanism, chains with more conformation disorders could greatly hinder either nucleation or growth of the other form in the crystallization minimum region.

Using a framework similar to polymorphs observed in one of the PE-like polymers,[48] in our study of PA6, vibrational spectroscopy has confirmed that the three crystalline modifications have different conformations, and calorimetry data have confirmed that they have different degrees of stability. One more feature that PE-like polymers[48] and PA6 share is that the kinetic discontinuity is always found just below the melting temperature of the less stable form. The low undercooling results in a low thermodynamic drive to nucleate, so the more stable form can gradually become the dominant phase. As shown in Figure 11, t_{peak} associated with β-phase formation starts to decrease at 105 °C, which is just below the observed melting temperature of the β-phase. In the meantime, the γ-phase starts to develop. However, a unique observation in the current work is that the discontinuity is seen on the low-temperature side described in the Turnbull−Fisher equation, where the mobility of chain segments plays a major role in affecting crystallization. The more stable form γ-phase appears earlier than the β-phase, as extracted from the t_{peak} data. The chain attachment that occurred on the lamellar surface of the γ-phase does not follow the temporary block phenomena

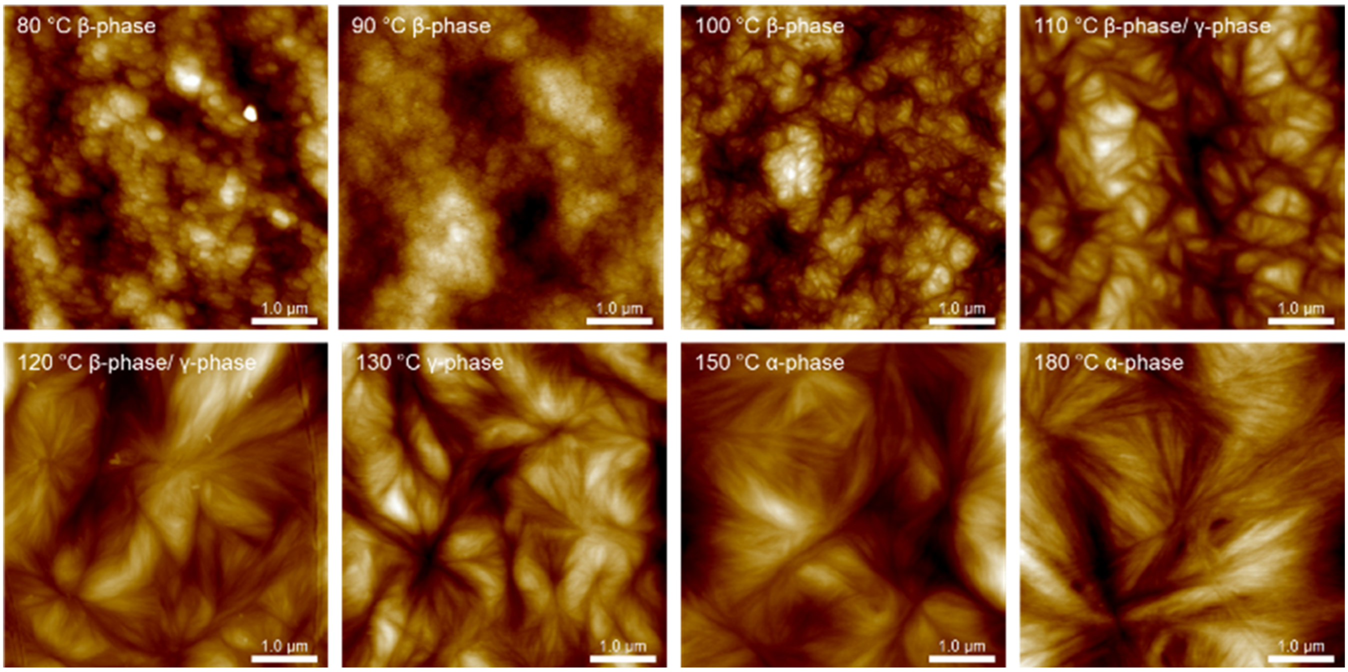

Figure 13. AFM images of PA6 isothermally melt-crystallized at indicated temperatures. The micrographs were collected in a 5 × 5 μm^2 area using height mode.

described in PE-like molecules. In other words, the nucleation and growth of the γ-phase might not be affected by the formation of the β-phase. This explains why no drastic crystallization rate minimum of the γ-phase was found in the transition region. Instead, the discontinuity can be simply explained by the different temperature coefficients of the crystallization kinetics of the β- and γ-phase.

The kinetic discontinuities in iPP,[33,68] PCL,[34] and PA11[31] were also explained by the change of the nucleation mechanism from homogenous nucleation to heterogeneous nucleation. It is noted that typical morphology analysis of polymers using a combined FSC and AFM approach only studied morphology at high and low supercooling extremes because the FSC sensor membrane needed to be fractured to obtain the sample for AFM measurements. This practice is an expensive endeavor, so only a few images are typically taken per sample studied. It is typically hypothesized that a distinct transition from heterogeneous to homogeneous nucleation is judged by a local minimum in the crystallization rate as found by the calorimetry measurements. To examine the transition between different nucleation mechanisms at a kinetics discontinuity, micron- and nanoscale morphology over the full crystallization temperature spectrum was collected for the first time by direct measurements on the FSC membrane without fracture.

Morphology Changes. The morphology after isothermal crystallization on the FSC chip was first examined using polarized optical microscopy. The set of micrographs shown in Figure 12 demonstrates a clear change from the mesomorphic β-phase to γ- and α-phases. When PA6 was crystallized at temperatures of 80 and 100 °C, the corresponding micrographs collected without the retardation plate were fully dark. These micrographs are indistinguishable from the one from the amorphous sample, indicating that the mesophase develops a profuse number of transparent crystals under visible light. The reason for the transparent sample is that the crystals or aggregates have a size near or below the wavelength of visible light. More details of crystals or aggregate sizes are displayed in Figure S4. When the crystallization temperature is no longer in the β-phase region, very few crystals become visible. The crystals' size and birefringence continue to increase with higher crystallization temperature, as shown in Figure 12. At 180 °C, space-filling spherulitic superstructures with a size up to 5 μm are visible.

In order to further explore the morphology at the submicron scale, AFM was utilized for imaging of PA6 after isothermal crystallization across a wide temperature range. Unlike previous work by Mileva *et al.* on PA6,[17] the AFM experiments were carried out directly on the UFS1 membrane without detaching it from the silicon frame and the ceramic housing. The same region of the PA6 sample can be scanned directly after introducing different thermal histories. This allows for a series of images to be produced on the same polymer, eliminating the variables that may come with using a different sample for each morphological measurement. The AFM images of samples that crystallized at temperatures from 80 to 180 °C are displayed in Figure 13.

The morphology of PA6 at different T_c values undergoes two stages of changes, as shown in Figure 13. The first stage of morphology change occurs at T_c below 120 °C. The AFM image of PA6 crystallized at 80 °C shows a typical particle-like, nodular morphology. At T_c of 90 °C or higher, crystal aggregates (clusters) can be identified. A lower number of crystal aggregates with smoother surfaces are found at higher crystallization temperatures. Fewer crystal aggregates observed at higher T_c are due to lower thermodynamic driving forces when approaching the melting temperature of the β-phase. At 110 °C, the highest T_c that the β-phase can form, even though the crystal aggregates have an average size of around 1 μm, no clear centers of aggregates or spherulitic structures are found. The second stage of morphology change occurs between 110 and 120 °C, where the γ-phase quickly becomes the dominant

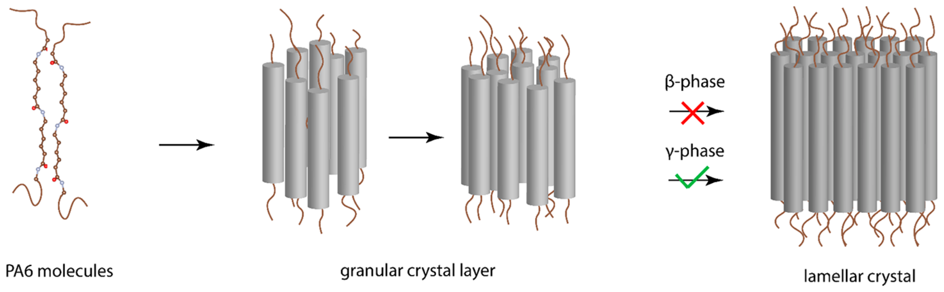

Figure 14. Schematic illustration of crystal growth of PA6 in the case of the β-phase and the γ-phase (not to scale). Each gray tube represents a conformational ordered segment of the PA6 molecule. There is no transition from the granular crystal layer to the lamellar crystal below 120 °C.

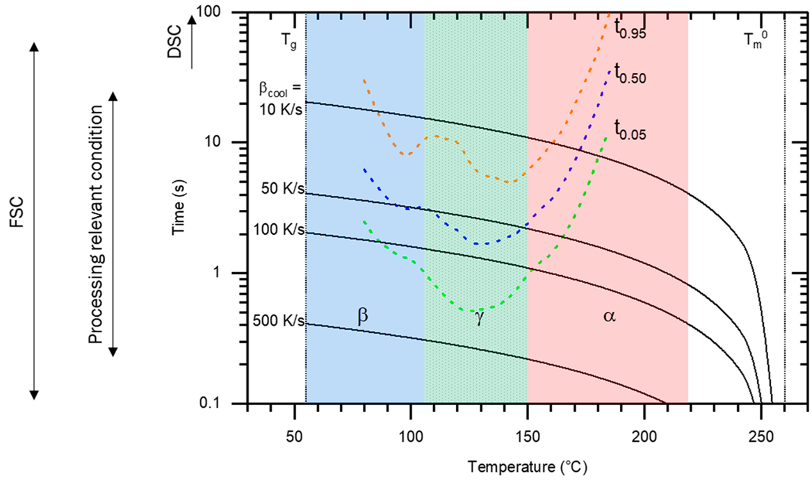

Figure 15. TTT diagram for PA6 crystallized from the melt. $t_{0.05}$, $t_{0.50}$, and $t_{0.95}$ are the time for 5, 50, and 95% transformation, respectively. The temperature−time variations at a constant cooling rate of 10, 50, 100, and 500 °C/s are added.

phase. When the crystallization temperature is 120 °C or above, only spherulites consisting of arrays of lamellae develop. In the meantime, the nucleation density drops significantly. The abrupt morphology change between 110 and 120 °C follows the prediction of switching nucleation mechanisms that were used to explain observations in iPP,[33,68] PCL,[37] and PA11.[31] However, it is unclear why the role of nucleants suddenly changes in the polymorphic region of β-/γ-phases of PA6.

An alternative model, the multistage growth model initially proposed by Strobl,[77] can explain the two-stage morphology changes observed in PA6. In the multistage model, the crystal growth starts with the attachment of stems from the melt to form a mesomorphic layer. With continuous solidification, the mesomorphic layer forms a granular crystal layer. The thickening process requires a continuous rearrangement of the chain sequence at the cost of mobility. When the mobility is high enough, it is possible to form lamellar crystals from the granular crystal layer. The proposed model has been supported by many recent works.[77−81] As illustrated in Figure 14, the gradual morphology change of PA6 in the β-phase region can be interpreted as the transition stopping at the granular crystal stage because of the low mobility. The lack of the lamellar structure halts the radial growth of the crystal. This can explain why no lamellar structure and spherulitic structures were observed in the β-phase region. However, as suggested by the reduced surface roughness, the tendency to form lamellar crystals from the granular crystal stage increases when the crystallization temperature approaches 120 °C. At 120 °C, the chains' mobility is high enough to rearrange themselves to form a more ordered γ-phase, which finally enables the formation of lamellar crystals. In the paper by Xu *et al.*, they annealed the PA6 β-phase and started to observe a weak disperse SAXS peak at 120 °C,[8] the same temperature where the lamellar structure first appears from isothermal crystallization experiments. Their experiments also demonstrated that the transition from the granular crystal layer to form structures with long-range order could also be achieved by annealing, as long as the mobility of the PA6 chain is high enough.

Phase Diagram of PA6 at Processing-Relevant Conditions. A survey of previous research reveals many controversies and ambiguity of structural habits and thermodynamic properties published in the literature, mainly with respect to the pseudo-hexagonal β- and γ-phases. The contradictory observations regarding the two pseudo-hexagonal phases of PA6 are believed to be associated with the high sensitivity of polymorphism transitions to processing conditions. Because conventional differential scanning calorimeters or hot stage techniques are unable to cool PA6 at very high rates, the low-temperature crystallization studies of PA6 in the past had to take samples from melt-spun fibers or blown and cast films formed on a chill roll. The high-speed cooling typically studied in manufactured specimens cannot differentiate between cooling-induced or shear-induced crystal forms. Undesired flow-induced crystallization is now no longer an issue because of the development of the FSC, allowing the cooling rate and temperature dependence of the crystallization process to be selectively studied. The combination of calorimetry, scattering, spectroscopy, and morphological characterization on a single chip has been demonstrated to

https://doi.org/10.1021/acs.macromol.1c00811
Macromolecules 2021, 54, 7512−7528

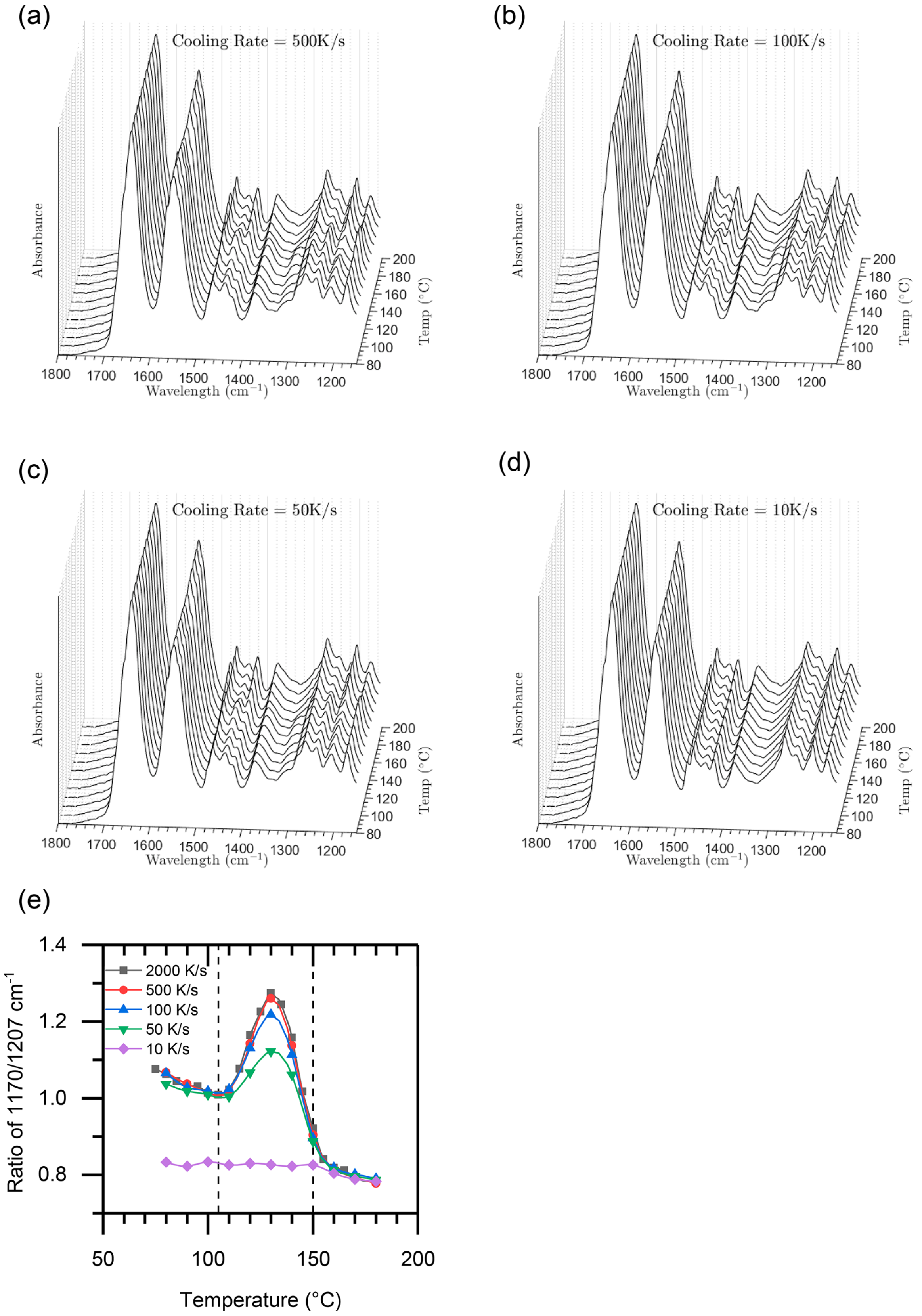

Figure 16. FTIR spectra in the region of 1800−1150 cm^{-1} of PA6 after isothermal crystallization using indicated rates (a−d). Their corresponding variations of the (e) peak ratio of 1170/1206 cm^{-1} bands are plotted.

be effective in understanding the phase diagram of PA6 at ultrafast cooling conditions up to 2000 K/s. Here, the effect of processing conditions on the final phase diagram of PA6 is also explored.

A TTT diagram for the crystallization of PA6 is built as illustrated in Figure 15. In addition to the half-transformation time, the time of transformation at 5 and 95%, $t_{0.05}$ and $t_{0.95}$, were extracted from the heat of fusion data using the following formula derived from the logistic equation, where p is the same fitting parameter used in the interruption method.

$$t = \frac{t_{0.5}}{\left(\frac{1}{y} - 1\right)^{1/p}}$$

In the formula, y is 0.05 and 0.95 for 5 and 95% conversions, respectively. Here, it is assumed that the crystallization starts and almost completes after reaching $t_{0.05}$ and $t_{0.95}$, respectively. In order to represent different cooling pathways semi-quantitatively, the time to cool from the equilibrium melting temperature to a given temperature is calculated using the following equation.

$$t = \frac{T_{\mathrm{final}} - T_{\mathrm{m}}^{0}}{\beta_{\mathrm{cool}}}$$

where t is the time to reach temperature T_{final} using a constant cooling rate of β_{cool}. The equation assumes that the crystallization takes place immediately after the sample is cooled below an equilibrium melting temperature $T_m{}^0$ of 260 °C[10] and above a glass transition temperature of 55 °C. The real process is, of course, more complicated because the early stage of crystallization needs to surmount the free energy barrier. Because of the energy barrier, the crystallization peak is always observed a few degrees below the melting peak. The crystallization in a real case should start to happen at a few degrees below T_{m}^{0}. Using the abovementioned equation, the cooling pathways of 10, 50, 100, and 500 K/s are calculated in the same figure of the TTT diagram. These cooling rates commonly occur in injection molding and extrusion processes, with the cooling rate dependent upon the distance from the cooled surface. The cooling pathway of 2000 K/s used in the previous section cannot be shown in this diagram because it only takes 0.1 s to cool from 260 to 60 °C. In order to examine the effect of the cooling rate on the polymorph formation, the temperature-dependent spectra using the same cooling rates before isothermal crystallization were also collected, as displayed in Figure 16. The peak ratio of 1170/1207 cm^{-1} bands, as demonstrated previously, is sensitive to the three forms. Here, the ratio is used to characterize the three phases under different cooling pathways.

As shown in Figure 15, the cooling pathway of 500 K/s does not intercept with the curve of $t_{0.05}$, which means that the crystallization has not started yet across the entire temperature span. Therefore, the sample crystallized at the given T_c has no contamination of other crystals formed during cooling. At the rate of 100 K/s, the cooling is not fast enough to fully bypass the crystallization region. The representative cooling curve at this rate intercepts with the $t_{0.05}$ curve in the α-phase region but not with the $t_{0.50}$ and $t_{0.95}$ curves. Considering the free energy barrier for nucleation, the material crystallized below the intercept temperature around 150 °C may have tiny or almost no contribution from the α-phase. In both cases of cooling at 500 and 100 K/s, PA6 is mostly amorphous after reaching the given crystallization temperature, so the contribution sometimes is not significant enough to be reflected in the corresponding spectra. As illustrated in Figure 16, the temperature-dependent spectra collected using rates of 500 and 100 K/s are almost identical to those collected using a rate of 2000 K/s. The corresponding peak ratios of 1170/1207 cm^{-1} bands are almost indistinguishable from the data using a higher cooling rate of 2000 K/s. It is noted that in real processing conditions, for example, in melt-spinning of fibers, the cooling rate should vary with the linear mass density of fibers and the temperature gradient according to the laws of heat transfer. Using such conditions, the formation of β- or γ-phases from melt crystallization is possible. This can explain the controversies and ambiguity of structural features in the previous studies. When the cooling rate is 50 K/s or below, most of the transformation has been completed during cooling. The observed WAXS diffractograms or FTIR spectra using this condition will inevitably include crystals from the α-phase. As illustrated in Figure 16, PA6 spectra after cooling at a rate of 10 K/s are identical to that characteristic of the α-phase spectrum. The measured peak ratios of 1170/1207 cm^{-1} bands are independent of the crystallization temperature. Unfortunately, a cooling rate of 10 K/s is still beyond the highest rate that most differential scanning calorimeters and hot stages can achieve. Therefore, it is not surprising that in some studies, polymorphism transitions cannot be easily seen in PA6[23] because the thermodynamically stable α-phase is the dominant phase.

CONCLUSIONS

In summary, the different polymorphs in PA6 crystallized from the melt and their associated spectroscopic, crystallization kinetics, and morphological behavior have been studied. This goal was achieved by using a novel integrated FSC chip allowing vibrational spectroscopy characterization. The modified FSC chip enables the authors, for the first time, to cool and heat PA6 samples at an ultrahigh rate to the desired temperature to perform nondamaging repeatable morphology characterizations on a UFS1-type chip.

Three polymorphs of melt-crystallized PA6 are easily distinguished by frequency shifting and absorbance changes of amide- and methylene-related bands. The mesomorphic β-phase develops below 105 °C and the α-phase forms above 150 °C. The formation of the γ-phase from the melt has been confirmed because the spectrum collected at 130 °C exhibits all the features seen in the PA6 γ-phase prepared from KI/I_2 solution. In the temperature between 105 and 150 °C, the γ-phase coexists with the β- or α-phases.

The overall crystallization rates of PA6 extracted from crystallization exothermic peaks, or the interruption method, display the usual temperature coefficient in the region where only one phase develops. In the transition region between the β-/γ-phase, crystallization kinetics exhibit a discontinuity. It is suggested that this discontinuity is caused by different temperature-coefficients of the β- and γ-phase. In contrast, the data extracted from cold crystallization only show a monomodal distribution of the t_{peak} values.

PA6 exhibits two types of morphologies at different T_c values. At T_c below 120 °C, a lower number of crystal aggregates with smoother surfaces are found at higher crystallization temperatures. An abrupt morphology change occurs between 110 and 120 °C, where the γ-phase quickly becomes the dominant phase. At T_c of 120 °C or above, only spherulites consisting of arrays of lamellae develop. The sudden morphology change confirms the prediction of switching nucleation mechanisms. The two types of morphology changes can be explained by the multistage growth model.

The TTT diagram constructed by kinetics data coupled with different cooling pathways reveals that the formation of three phases also depends on the cooling rate. If the cooling rate exceeds 500 K/s, the crystallization is fully bypassed. The subsequent isothermal crystallization is free from the other polymorphs. When the cooling rate is equal to or lower than 100 K/s, crystallization occurs before reaching low crystallization temperatures. At a rate of 10 K/s, only the α-phase can develop regardless of the isothermal crystallization. The data suggest that poor control of the cooling pathways can lead to contradictory and ambiguous observations of crystalline behaviors of PA6. The novel experimental platform approach adopted in this work relies on a modified FSC chip and has been proven to be a powerful tool to study polymer crystallization across a wide spectrum of heating and cooling rates, including those that encompass engineering-relevant polymer processing conditions.

■ ASSOCIATED CONTENT

Supporting Information

The Supporting Information is available free of charge at https://pubs.acs.org/doi/10.1021/acs.macromol.1c00811.

> FSC heating curves after cooling using different rates; estimation and subtraction of the fringe pattern from the spectrum of SiN_x; frequencies and assignments of major bands of PA6 α-, γ-, and β-phases; waterfall plot of heat flow during isothermal crystallization of PA6 on a regular FSC chip; and estimation of crystal or aggregate sizes using AFM micrographs (PDF)

■ AUTHOR INFORMATION

Corresponding Author

Alicyn M. Rhoades − *School of Engineering, Penn State Behrend, Erie, Pennsylvania 16563, United States;* orcid.org/0000-0003-4678-419X; Email: amh234@psu.edu

Authors

Xiaoshi Zhang − *School of Engineering, Penn State Behrend, Erie, Pennsylvania 16563, United States;* orcid.org/0000-0002-5281-6285

Anne Gohn − *School of Engineering, Penn State Behrend, Erie, Pennsylvania 16563, United States*

Gamini Mendis − *School of Engineering, Penn State Behrend, Erie, Pennsylvania 16563, United States*

John F. Buzinkai − *INVISTA, Wichita, Kansas 67220, United States*

Steven J. Weigand − *DND-CAT Synchrotron Research Center, Northwestern University, Argonne, Illinois 60439, United States*

Complete contact information is available at: https://pubs.acs.org/10.1021/acs.macromol.1c00811

Funding

This research was funded by INVISTA and supported by the National Science Foundation (Grant no. 1653629).

Notes

The authors declare no competing financial interest.

■ ACKNOWLEDGMENTS

The authors would like to thank the DuPont-Northwestern-Dow Collaborative Access Team (DND-CAT) located at Sector 5 of the Advanced Photon Source (APS) at Argonne National Laboratory (ANL). The discussion with Gregory P. Dillon, René Androsch, and Ralph Colby is gratefully acknowledged.

■ REFERENCES

(1) Cheng, S. Z. D.; Lotz, B. Enthalpic and entropic origins of nucleation barriers during polymer crystallization: the Hoffman-Lauritzen theory and beyond. *Polymer* **2005**, *46*, 8662−8681.

(2) Seguela, R. Overview and Critical Survey of Polyamide6 Structural Habits: Misconceptions and Controversies. *J. Polym. Sci* **2020**, *58*, 2971−3003.

(3) Murthy, N. S. Metastable Crystalline Phases in Nylon 6. *Polym. Commun.* **1991**, *32*, 301−305.

(4) Arimoto, H.; Ishibashi, M.; Hirai, M.; Chatani, Y. Crystal structure of the γ-form of nylon 6. *J. Polym. Sci., A* **1965**, *3*, 317−326.

(5) Ogawa, M.; Ōta, T.; Yoshizaki, O.; Nagai, E. Notes on Nylon 6 Single Crystal. *J. Polym. Sci., Part B: Polym. Lett.* **1963**, *1*, 57−61.

(6) Kyotani, M. Solution Crystallization of Nylon 6. *J. Polym. Sci., Polym. Phys. Ed.* **1979**, *17*, 103−114.

(7) Auriemma, F.; Petraccone, V.; Parravicini, L.; Corradini, P. Mesomorphic Form(β) of Nylon 6. *Macromolecules* **1997**, *30*, 7554−7559.

(8) Xu, J.-R.; Ren, X.-K.; Yang, T.; Jiang, X.-Q.; Chang, W.-Y.; Yang, S.; Stroeks, A.; Chen, E.-Q. Revisiting the Thermal Transition of β-Form Polyamide-6: Evolution of Structure and Morphology in Uniaxially Stretched Films. *Macromolecules* **2018**, *51*, 137−150.

(9) Androsch, R.; Stolp, M.; Radusch, H.-J. Crystallization of Amorphous Polyamides from the Glassy State. *Acta Polym.* **1996**, *47*, 99−104.

(10) Illers, V. K.-H.; Haberkorn, H. Schmelzverhalten, struktur und kristallinität von 6-polyamid. *Makromol. Chem.* **1971**, *142*, 31−67.

(11) Stepaniak, R. F.; Garton, A.; Carlsson, D. J.; Wiles, D. M. An Examination of the Crystal Structures Present in Nylon-6 Fibers. *J. Polym. Sci., Polym. Phys. Ed.* **1979**, *17*, 987−999.

(12) Vasanthan, N. Orientation and Structure Development in Polyamide 6 Fibers upon Drawing. *J. Polym. Sci., Part B: Polym. Phys.* **2003**, *41*, 2870−2877.

(13) Murthy, N. S.; Aharoni, S. M.; Szollosi, A. B. Stability of the γ form and the development of the α form in nylon 6. *J. Polym. Sci., Polym. Phys. Ed.* **1985**, *23*, 2549−2565.

(14) Khanna, Y. P.; Kuhn, W. P. Measurement of Crystalline Index in Nylons by DSC: Complexities and Recommendations. *J. Polym. Sci., Part B: Polym. Phys.* **1997**, *35*, 2219−2231.

(15) Penel-Pierron, L.; Depecker, C.; Séguéla, R.; Lefebvre, J.-M. Structural and Mechanical Behavior of Nylon 6 Films Part I. Identification and Stability of the Crystalline Phases. *J. Polym. Sci., Part B: Polym. Phys.* **2001**, *39*, 484−495.

(16) van Drongelen, M.; Meijer-Vissers, T.; Cavallo, D.; Portale, G.; Poel, G. V.; Androsch, R. Microfocus Wide-Angle X-Ray Scattering of Polymers Crystallized in a Fast Scanning Chip Calorimeter. *Thermochim. Acta* **2013**, *563*, 33−37.

(17) Mileva, D.; Androsch, R.; Zhuravlev, E.; Schick, C. Morphology of Mesophase and Crystals of Polyamide 6 Prepared in a Fast Scanning Chip Calorimeter. *Polymer* **2012**, *53*, 3994−4001.

(18) Itoh, T.; Miyaji, H.; Asai, K. Thermal Properties of α- and γ-Forms of Nylon 6. *Jpn. J. Appl. Phys* **1975**, *14*, 206−215.

(19) Ramesh, C.; Gowd, E. B. High-Temperature X-ray Diffraction Studies on the Crystalline Transitions in the α- and γ-Forms of Nylon-6. *Macromolecules* **2001**, *34*, 3308−3313.

(20) Illers, K.-H. Polymorphie, kristallinität und schmelzwärme von poly(ε-caprolactam), 2. Kalorimetrische untersuchungen. *Makromol. Chem.* **1978**, *179*, 497−507.

(21) Simak, P. Polymorphie, Kristallinität und Schmelzwärme von Poly(ε-caprolactam), 1. IR-spektroskopische Untersuchungen. *Makromol. Chem.* **1977**, *178*, 2927−2937.

(22) Murthy, N. S.; Curran, S. A.; Aharoni, S. M.; Minor, H. Premelting Crystalline Relaxations and Phase Transitions in Nylon 6 and 6,6. *Macromolecules* **1991**, *24*, 3215−3220.

(23) Vasanthan, N.; Murthy, N. S.; Bray, R. G. Investigation of Brill Transition in Nylon 6 and Nylon 6,6 by Infrared Spectroscopy. *Macromolecules* **1998**, *31*, 8433−8435.

(24) Quarti, C.; Milani, A.; Civalleri, B.; Orlando, R.; Castiglioni, C. Ab Initio Calculation of the Crystalline Structure and IR Spectrum of Polymers: Nylon 6 Polymorphs. *J. Phys. Chem. B* **2012**, *116*, 8299−8311.

(25) Porter, R. S. Macromolecular physics, volume 3-crystal melting, Bernhard Wunderlich, Academic Press, New York, 1980, 363 pp. Price: $42.50. *J. Polym. Sci., Polym. Lett. Ed.* **1980**, *18*, 824.

(26) Pepin, J.; Miri, V.; Lefebvre, J.-M. New Insights into the Brill Transition in Polyamide 11 and Polyamide 6. *Macromolecules* **2016**, *49*, 564−573.

(27) Mileva, D.; Kolesov, I.; Androsch, R. Morphology of Cold-Crystallized Polyamide 6. *Colloid Polym. Sci.* **2012**, *290*, 971−978.

(28) Cavallo, D.; Gardella, L.; Alfonso, G. C.; Portale, G.; Balzano, L.; Androsch, R. Effect of Cooling Rate on the Crystal/Mesophase Polymorphism of Polyamide 6. *Colloid Polym. Sci.* **2011**, *289*, 1073−1079.

(29) Furushima, Y.; Nakada, M.; Ishikiriyama, K.; Toda, A.; Androsch, R.; Zhuravlev, E.; Schick, C. Two Crystal Populations with Different Melting/Reorganization Kinetics of Isothermally Crystallized Polyamide 6. *J. Polym. Sci., Part B: Polym. Phys.* **2016**, *54*, 2126−2138.

(30) Rhoades, A. M.; Williams, J. L.; Androsch, R. Crystallization Kinetics of Polyamide 66 at Processing-Relevant Cooling Conditions and High Supercooling. *Thermochim. Acta* **2015**, *603*, 103−109.

(31) Mollova, A.; Androsch, R.; Mileva, D.; Schick, C.; Benhamida, A. Effect of Supercooling on Crystallization of Polyamide 11. *Macromolecules* **2013**, *46*, 828−835.

(32) Androsch, R.; Rhoades, A. M.; Stolte, I.; Schick, C. Density of Heterogeneous and Homogeneous Crystal Nuclei in Poly (Butylene Terephthalate). *Eur. Polym. J.* **2015**, *66*, 180−189.

(33) de Santis, F.; Adamovsky, S.; Titomanlio, G.; Schick, C. Isothermal Nanocalorimetry of Isotactic Polypropylene. *Macromolecules* **2007**, *40*, 9026−9031.

(34) Wurm, A.; Zhuravlev, E.; Eckstein, K.; Jehnichen, D.; Pospiech, D.; Androsch, R.; Wunderlich, B.; Schick, C. Crystallization and Homogeneous Nucleation Kinetics of Poly(ε-caprolactone) (PCL) with Different Molar Masses. *Macromolecules* **2012**, *45*, 3816−3828.

(35) Gohn, A. M.; Rhoades, A. M.; Wonderling, N.; Tighe, T.; Androsch, R. The Effect of Supercooling of the Melt on the Semicrystalline Morphology of PA 66. *Thermochim. Acta* **2017**, *655*, 313−318.

(36) Vasanthan, N.; Salem, D. R. FTIR Spectroscopic Characterization of Structural Changes in Polyamide-6 Fibers during Annealing and Drawing. *J. Polym. Sci., Part B: Polym. Phys.* **2001**, *39*, 536−547.

(37) Arimoto, H. α-γ Transition of nylon 6. *J. Polym. Sci., Part A: Gen. Pap.* **1964**, *2*, 2283−2295.

(38) Nair, S. S.; Ramesh, C. Studies on the Crystallization Behavior of Nylon-6 in the Presence of Layered Silicates Using Variable Temperature WAXS and FTIR. *Macromolecules* **2005**, *38*, 454−462.

(39) van Herwaarden, S.; Iervolino, E.; van Herwaarden, F.; Wijffels, T.; Leenaers, A.; Mathot, V. Design, Performance and Analysis of Thermal Lag of the UFS1 Twin-Calorimeter Chip for Fast Scanning Calorimetry Using the Mettler-Toledo Flash DSC 1. *Thermochim. Acta* **2011**, *522*, 46−52.

(40) Holland, B. J.; Hay, J. N. Thermal Degradation of Nylon Polymers. *Polym. Int.* **2000**, *49*, 943−948.

(41) Anton, A. M.; Zhuravlev, E.; Kossack, W.; Andrianov, R.; Schick, C.; Kremer, F. Fingerprints of Homogeneous Nucleation and Crystal Growth in Polyamide 66 as Studied by Combined Infrared Spectroscopy and Fast Scanning Chip Calorimetry. *Colloid Polym. Sci.* **2020**, *298*, 697−706.

(42) Hill, A. V. The Possible Effects of the Aggregation of the Molecules of Hæmoglobin on Its Dissociation Curves. *J. Physiol.* **1910**, *40*, i−vii.

(43) Guan, Y.; Yang, S.; Zhang, Y.; Xu, J.; Han, C. C.; Kotov, N. A. Fabry−Perot Fringes and Their Application To Study the Film Growth, Chain Rearrangement, and Erosion of Hydrogen-Bonded PVPON/PAA Films. *J. Phys. Chem. B* **2006**, *110*, 13484−13490.

(44) Konevskikh, T.; Ponossov, A.; Blümel, R.; Lukacs, R.; Kohler, A. Fringes in FTIR Spectroscopy Revisited: Understanding and Modelling Fringes in Infrared Spectroscopy of Thin Films. *Analyst* **2015**, *140*, 3969−3980.

(45) Azarfar, G.; Aboualizadeh, E.; Walter, N. M.; Ratti, S.; Olivieri, C.; Norici, A.; Nasse, M.; Kohler, A.; Giordano, M.; Hirschmugl, C. J. Estimating and Correcting Interference Fringes in Infrared Spectra in Infrared Hyperspectral Imaging. *Analyst* **2018**, *143*, 4674−4683.

(46) Holmes, D. R.; Bunn, C. W.; Smith, D. J. The Crystal Structure of Polycaproamide: Nylon 6. *J. Polym. Sci.* **1955**, *17*, 159−177.

(47) Zhang, X.; Zuo, X.; Ortmann, P.; Mecking, S.; Alamo, R. G. Crystallization of Long-Spaced Precision Polyacetals I: Melting and Recrystallization of Rapidly Formed Crystallites. *Macromolecules* **2019**, *52*, 4934−4948.

(48) Zhang, X.; Marxsen, S. F.; Ortmann, P.; Mecking, S.; Alamo, R. G. Crystallization of Long-Spaced Precision Polyacetals II: Effect of Polymorphism on Isothermal Crystallization Kinetics. *Macromolecules* **2020**, *53*, 7899−7913.

(49) Kolesov, I.; Mileva, D.; Androsch, R.; Schick, C. Structure Formation of Polyamide 6 from the Glassy State by Fast Scanning Chip Calorimetry. *Polymer* **2011**, *52*, 5156−5165.

(50) Li, Y.; Goddard, W. A. Nylon 6 Crystal Structures, Folds, and Lamellae from Theory. *Macromolecules* **2002**, *35*, 8440−8455.

(51) Murthy, N. S. Hydrogen Bonding, Mobility, and Structural Transitions in Aliphatic Polyamides. *J. Polym. Sci., Part B: Polym. Phys.* **2006**, *44*, 1763−1782.

(52) Murthy, N. S.; Stamm, M.; Sibilia, J. P.; Krimm, S. Structural Changes Accompanying Hydration in Nylon 6. *Macromolecules* **1989**, *22*, 1261−1267.

(53) Yoshioka, Y.; Tashiro, K. Structural Changes in Phase Transitions of Nylon Model Compounds. 1. Transition Behavior of Model Compounds of R-NHCO-R' Type. *J. Phys. Chem. B* **2003**, *107*, 11835−11842.

(54) Yoda, N.; Miyake, A. Polymerization of α-piperidone by alkali metal and certain acyl compounds. *J. Polym. Sci.* **1960**, *43*, 117−136.

(55) Matsubara, I.; Magill, J. H. An infra-red study of the interaction of polyamides with iodine in iodine-potassium iodide solution. *Polymer* **1966**, *7*, 199−215.

(56) Heidemann, V. G.; Zahn, H. Beitrag Zur Deutung Des Infrarotspektrums von Nylon 6,6. *Makromol. Chem.* **1963**, *62*, 123−133.

(57) Rotter, G.; Ishida, H. FTIR separation of nylon-6 chain conformations: Clarification of the mesomorphous and γ-crystalline phases. *J. Polym. Sci., Part B: Polym. Phys.* **1992**, *30*, 489−495.

(58) Cooper, S. J.; Coogan, M.; Everall, N.; Priestnall, I. A polarised μ-FTIR study on a model system for nylon 6 6: implications for the nylon Brill structure. *Polymer* **2001**, *42*, 10119−10132.

(59) Simon, P.; Argay, G. Revised Atomic Coordinates of Crystalline Nylon-6. *J. Polym. Sci., Polym. Phys. Ed.* **1978**, *16*, 935−937.

(60) Klaus, J. W.; Ott, A. W.; Dillon, A. C.; George, S. M. Atomic Layer Controlled Growth of Si3N4 Films Using Sequential Surface Reactions. *Surf. Sci.* **1998**, *418*, L14−L19.

(61) Jakeš, J.; Krimm, S. Normal Coordinate Analyses of Molecules with the Amide Group. *Spectrochim. Acta, Part A* **1971**, *27*, 35−63.

(62) Fontana, L.; Santoro, M.; Bini, R.; Vinh, D. Q.; Scandolo, S. High-Pressure Vibrational Properties of Polyethylene. *J. Chem. Phys.* **2010**, *133*, 204502.

(63) Zhang, X.; Santonja-Blasco, L.; Wagener, K. B.; Boz, E.; Tasaki, M.; Tashiro, K.; Alamo, R. G. Infrared Spectroscopy and X-Ray Diffraction Characterization of Dimorphic Crystalline Structures of Polyethylenes with Halogens Placed at Equal Distance along the Backbone. *J. Phys. Chem. B* **2017**, *121*, 10166−10179.

(64) Li, H.-W.; Strauss, H. L.; Snyder, R. G. Differences in the IR Methylene Rocking Bands between the Crystalline Fatty Acids and n-Alkanes: Frequencies, Intensities, and Correlation Splitting. *J. Phys. Chem. A* **2004**, *108*, 6629−6642.

(65) Xu, J.-R.; Ren, X.-K.; Yang, T.; Jiang, X.-Q.; Chang, W.-Y.; Yang, S.; Stroeks, A.; Chen, E.-Q. Revisiting the Thermal Transition of β-Form Polyamide-6: Evolution of Structure and Morphology in Uniaxially Stretched Films. *Macromolecules* **2018**, *51*, 137−150.

(66) Turnbull, D.; Fisher, J. C. Rate of Nucleation in Condensed Systems. *J. Chem. Phys.* **1949**, *17*, 71−73.

(67) Seo, J.; Gohn, A. M.; Dubin, O.; Takahashi, H.; Hasegawa, H.; Sato, R.; Rhoades, A. M.; Schaake, R. P.; Colby, R. H. Isothermal Crystallization of Poly(Ether Ether Ketone) with Different Molecular Weights over a Wide Temperature Range. *Polym. Cryst.* **2019**, *2*, No. e10055.

(68) Schawe, J. E. K.; Pötschke, P.; Alig, I. Nucleation Efficiency of Fillers in Polymer Crystallization Studied by Fast Scanning Calorimetry: Carbon Nanotubes in Polypropylene. *Polymer* **2017**, *116*, 160−172.

(69) Supaphol, P.; Spruiell, J. E. Isothermal Melt- and Cold-Crystallization Kinetics and Subsequent Melting Behavior in Syndiotactic Polypropylene: A Differential Scanning Calorimetry Study. *Polymer* **2001**, *42*, 699−712.

(70) Kawai, T.; Rahman, N.; Matsuba, G.; Nishida, K.; Kanaya, T.; Nakano, M.; Okamoto, H.; Kawada, J.; Usuki, A.; Honma, N.; Nakajima, K.; Matsuda, M. Crystallization and Melting Behavior of Poly (l-Lactic Acid). *Macromolecules* **2007**, *40*, 9463−9469.

(71) Ungar, G.; Putra, E. G. R.; de Silva, D. S. M.; Shcherbina, M. A.; Waddon, A. J. The Effect of Self-Poisoning on Crystal Morphology and Growth Rates. *Adv. Polym. Sci.* **2005**, 45−87.

(72) Kovacs, A. J.; Straupe, C. Isothermal Growth, Thickening and Melting of Poly(Ethylene-Oxide) Single Crystals in the Bulk. *J. Cryst. Growth* **1980**, *48*, 210−226.

(73) Zhang, X.; Zhang, W.; Wagener, K. B.; Boz, E.; Alamo, R. G. Effect of Self-Poisoning on Crystallization Kinetics of Dimorphic Precision Polyethylenes with Bromine. *Macromolecules* **2018**, *51*, 1386−1397.

(74) Ungar, G.; Keller, A. Inversion of the Temperature Dependence of Crystallization Rates Due to Onset of Chain Folding. *Polymer* **1987**, *28*, 1899−1907.

(75) Organ, S. J.; Ungar, G.; Keller, A. Rate Minimum in Solution Crystallization of Long Paraffins. *Macromolecules* **1989**, *22*, 1995−2000.

(76) Boda, E.; Ungar, G.; Brooke, G. M.; Burnett, S.; Mohammed, S.; Proctor, D.; Whiting, M. C. Crystallization Rate Minima in a Series of N-Alkanes from $C_{194}H_{390}$ to $C_{294}H_{590}$. *Macromolecules* **1997**, *30*, 4674−4678.

(77) Strobl, G. From the Melt via Mesomorphic and Granular Crystalline Layers to Lamellar Crystallites: A Major Route Followed in Polymer Crystallization? *Eur. Phys. J. E* **2000**, *3*, 165−183.

(78) Strobl, G. Crystallization and Melting of Bulk Polymers: New Observations, Conclusions and a Thermodynamic Scheme. *Prog. Polym. Sci.* **2006**, *31*, 398−442.

(79) Cong, Y.; Hong, Z.; Qi, Z.; Zhou, W.; Li, H.; Liu, H.; Chen, W.; Wang, X.; Li, L. Conformational Ordering in Growing Spherulites of Isotactic Polypropylene. *Macromolecules* **2010**, *43*, 9859−9864.

(80) Cong, Y.; Hong, Z.; Zhou, W.; Chen, W.; Su, F.; Li, H.; Li, X.; Yang, K.; Yu, X.; Qi, Z.; Li, L. Conformational Ordering on the Growth Front of Isotactic Polypropylene Spherulite. *Macromolecules* **2012**, *45*, 8674−8680.

(81) Magonov, S.; Godovsky, Y. Atomic Force Microscopy, Part 8: Visualization of Granular Nanostructure in Crystalline Polymers. *Am. Lab.* **1999**, *31*, 52.